AN ABSTRACT OF THE THESIS OF

Jesse A. Weller for the degree of Master of Science in Physics presented on June 2, 2021.

Title: Aberration Correction of Optical Wavefronts with Sequential, Genetic, and Deep Learning Algorithms

Abstract approved: _____

David H. McIntyre

In this work, we systematically explore the effectiveness of optical aberration correction over a wide range of optical depths using the Segmented and Zernike Polynomial bases. We manufacture a set of 16 optical phantom samples consisting of a clear polyester resin substrate embedded with varying concentrations of aluminum oxide (Al_2O_3) scattering particles. We measured the optical depth of the sample set, recording a range $\tau = 0 - 8.5$. Using these samples to distort a collimated laser wavefront, we conducted an experiment to determine the range of optical depths over which each optimization basis was effective. The results showed that the Zernike basis was more effective at low optical depths ($\tau < 1.5$), and the Segmented bases was more effective at higher optical depths ($\tau > 3$).

In a separate experiment, we trained a ResNet Convolutional Neural Network to correct for optical aberrations using single shot correction. First, we generated a

dataset of 8 million simulated optical aberrations using random phase modulation patterns, generated from a set of 34 Zernike Polynomials, loaded on to a liquid crystal spatial light modulator. We then applied a transfer learning technique to train an 18 layer ResNet neural network, pretrained on ImageNet, on the simulated dataset. Once trained, we tested the ability of the network to correct for new, randomly generated aberrations. Preliminary data showcases the trained network's ability to correct for new optical aberrations with high efficacy on a millisecond timescale.

Aberration Correction of Optical Wavefronts with Sequential, Genetic, and Deep Learning Algorithms

by

Jesse A. Weller

A THESIS

submitted to

Oregon State University

in partial fulfillment of
the requirements for the
degree of

Master of Science

Presented June 2, 2021
Commencement June 2022

Master of Science thesis of Jesse A. Weller presented on June 2, 2021.

APPROVED:

Major Professor, representing Physics

Head of the Department of Physics

Dean of the Graduate School

I understand that my thesis will become part of the permanent collection of Oregon State University libraries. My signature below authorizes release of my thesis to any reader upon request.

Jesse A. Weller, Author

ACKNOWLEDGEMENTS

Foremost, I would like to thank my advisor, David McIntyre, for giving me the opportunity, resources, and guidance to explore a topic of great interest to me. I would also like to express deep gratitude for the generosity of my many teachers and mentors here in the Physics Department, who have helped me grow personally, professionally, and scientifically over the last two years.

TABLE OF CONTENTS

LIST OF FIGURES

LIST OF FIGURES (Continued)

LIST OF FIGURES (Continued)

LIST OF TABLES

Chapter 1: Introduction

The use of light for imaging, manipulation, and stimulation is ubiquitous across all fields of science and medicine. Among the countless applications, it is employed to manipulate delicate micro-scale objects, probe the mechanics of the molecular and cellular environment, deliver light through opaque materials and within living tissues, and reveal hidden structure at the smallest and largest scales. In many of these applications, the ability to correct for aberrations in the optical system is crucial.

When light travels through a medium with spatial or temporal variations in its refractive index, distortions in the optical wavefront are induced. Left uncorrected, such distortions can severely degrade the image or focus quality in an optical system. For most of history, propagating media with severe aberrations were seen as an insurmountable obstacle to the effective control of light. However, with the invention of advanced filtering and adaptive optics techniques, it has become possible to overcome many of these limitations.

The field of Adaptive Optics (AO) grew out of efforts to correct for atmospheric aberrations in astronomical observation and satellite communication [1, 2]. The basic idea is to incorporate a deformable optical element into the imaging system which can be used to modulate the phase or amplitude pattern of imaging wavefront. Modern AO uses fast, high resolution active optical elements such

as digital micromirror devices and spatial light modulators (SLMs) that are able to modulate wavefronts with resolution at the micron scale. This has enabled enormous improvement and become mainstream in astronomical imaging, but AO techniques are also rapidly spreading into the fields of biological imaging and microscopy [3, 1, 4, 5, 6], where resolving smaller and smaller structures has become an imperative.

More recently, a sub-field of Adaptive Optics called Wavefront Shaping has emerged to address the correction of aberrations due to strongly scattering materials [7]. When passing through optically thick, disordered materials, the light from an incident wavefront is completely scrambled (Figure 1.1), creating a random speckle field in the output plane. The aberrations in such materials are scattering dominant and, until recently, were viewed as impossible to overcome. However, motivated by a statistical optics view of the problem [8, 9], it has been shown by many that focusing light through optically thick materials can be achieved by shaping the phase or amplitude pattern of the incident wavefront [10, 11, 12, 13]. The scattering effect of a medium can be overcome by modulating a plane wave in such a state that the transmission of the wave through the medium produces a desired intensity pattern.

1.1 Aberration Correction Domains

The distinction between the general Adaptive Optics correction domain and the specific correction domain addressed by Wavefront Shaping has to do with the

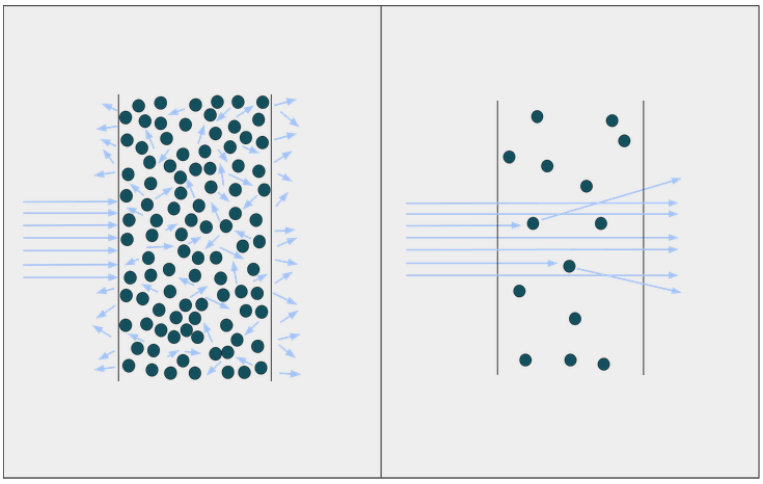

Figure 1.1: Optical Thickness. A collimated wavefront propagating through (left) an optically thick medium and (right) an optically thin medium.

severity and spatial frequency of the aberrations. In general AO, the media are generally optically thin with smooth, well ordered aberrations. This is why the Zernike Polynomial basis (see Section 1.3) is often used as the correction basis to optimize over. In the Zernike basis, the wavefront is decomposed into a set of two dimensional polynomials defined over the unit disc [14]. It was formulated to aid in characterizing common optical aberrations seen in the field of optometry, but it has since been applied to a wide range of correction problems across astronomy, photography, and microscopy [1]. Wavefront Shaping, on the other hand, employs the Segmented basis (see Section 2.2.3) modulation, which decomposes the wavefront into a set of spatially contiguous regions, usually rectangular in shape. In either approach, the aim is to find an optimal modulation pattern that, when applied to the laser wavefront, will correct for the aberrations induced by the distorting media and improve the image or focus quality.

Each approach has its own strengths and limitations depending on the optical domain. The Zernike basis provides a powerful representation of well ordered and highly symmetric optical aberrations, such as are present in weakly scattering, non-turbulent media. Because it was derived to include functions that describe patterns often found in optical tests, the Zernike basis enables efficient representation of these types of aberrations. However, the Zernike basis loses effectiveness in highly disordered media. The Segmented basis, alternatively, is able to correct for aberrations that are highly disordered. This is due to the spatial flexibility afforded by modulating over each region of the wavefront independently. The Segmented basis's weakness is that it requires a large number of modes (segments) to achieve a high quality fit for smooth, low order aberrations. In Chapter 2, we investigate the performance of each of these techniques at the overlap of the the two optical domains. We manufacture a set of optical phantoms with scattering dominated aberrations over a range of optical depths, from optically thin to optically thick (see Section 2.2.2). We then test the relative performance of aberration correction using the Segmented and Zernike bases over these set of phantoms, with the goal of more clearly delineating the correction domain over which each basis is effective.

1.2 Dynamic Aberrations and Single Shot Correction

Many of the traditional Adaptive Optics algorithms rely on a slow iterative optimization process, which has major limitations in systems where the aberrations are non-static. These types of aberrations are common in many astronomical and

biological domains due to the need to image through dynamic media such as living tissue or atmospheric fluctuations. In Chapter 3 we focus on the application of Deep Learning (DL) algorithms to this problem, which have the potential to greatly speed up the AO correction process. We build on previous work [15, 16, 17, 18] to develop a Convolutional Neural Network (CNN) model that can correct aberrations using a single measurement.

The basic idea is to train a CNN model on a large dataset of aberrated images, simulated by loading random Zernike Polynomial modulation patterns onto an optical elements. Since each aberrated image is generated from a known set of Zernike Polynomial coefficients, the network can be trained to predict the correct set of coefficients corresponding to each distorted intensity pattern. Once trained, the CNN model would then be able to take an unseen aberrated focus image as an input and output a set of Zernike coefficients that would refocus the beam. If successful, this method could enable millisecond timescale correction of dynamic aberrating media such as living tissue, turbulent liquids, or chaotic atmospheric fluctuations.

1.3 Zernike Polynomials

The Zernike basis comprises of a set of polynomials which are orthogonal over the unit disc [19, 14]. They can describe any sufficiently smooth and continuous optical aberration over the unit disc, requiring a relative few individual polynomials to achieve a high quality of correction. Out of the many possible two-dimensional

polynomial sets, Zernike Polynomials are often chosen for optical system correction in part because they describe many of the common aberrations in optical systems, such as Tip, Tilt, Defocus, Coma, Trefoil, Atigmatism, etc. (see Figure 1.2). In general, the Zernike Polynomials are described by,

$$Z_n^m(\rho,\varphi) = R_n^{|m|}(\rho) \cdot \begin{cases} \sin(|m|\varphi) & \text{if } m < 0, \\ 0 & \text{if } m = 0, \\ \cos(|m|\varphi) & \text{if } m > 0 \end{cases} \tag{1.1}$$

where $R_n^{|m|}$ are the radial Zernike polynomials. The indices n and m are the radial order and azimuthal order, respectively. The radial polynomials are described by the equation,

$$R_n^{|m|}(\rho) = \sum_{k=0}^{\frac{n-|m|}{2}} \frac{(-1)^k (n-k)!}{k!\left(\frac{n+|m|}{2}-k\right)!\left(\frac{n-|m|}{2}-k\right)!} \rho^{n-2k} \tag{1.2}$$

for all integers n,m such that $n \geq 0$, $|m| \leq n$, and $(n+m) \in even$. There are multiple formulations of the Zernike polynomials with differing indexing schemes. In this work, we used the Zernike Fringe Polynomials which are ordered by the spatial frequency $n + |m|$. In Figure 1.2, the first 15 polynomials are shown over the unit disc. For the Zernike Fringe Polynomials, one can generate the correct ordering of the polynomials by using the notation from Wyant and Creath [19], where the factoring of the radial Zernike polynomials,

$$R_{2n-|m|}^{|m|}(\rho) = Q_n^{|m|}(\rho)\rho^{|m|}, \tag{1.3}$$

leads to the ordering index j to be given by,

$$j = \left(1 + \frac{n + |m|}{2}\right)^2 - 2|m| + |sign(m)|\frac{1 - sign(m)}{2}. \tag{1.4}$$

The index j denotes the ordering of the polynomials $Z_n^m \rightarrow Z_j$. Equation 1.4 gives the Fringe index, which is equivalent to the Wyant index except that the Fringe index begins at $j = 1$, whereas the Wyant index begins at $j = 0$. This is as opposed to the completely different ordering given by the standard OSA/ANSI index,

$$j = \frac{n(n + 2) + m}{2}, \tag{1.5}$$

where the polynomials are ordered by the radial order n instead of spatial frequency $(n + |m|)$.

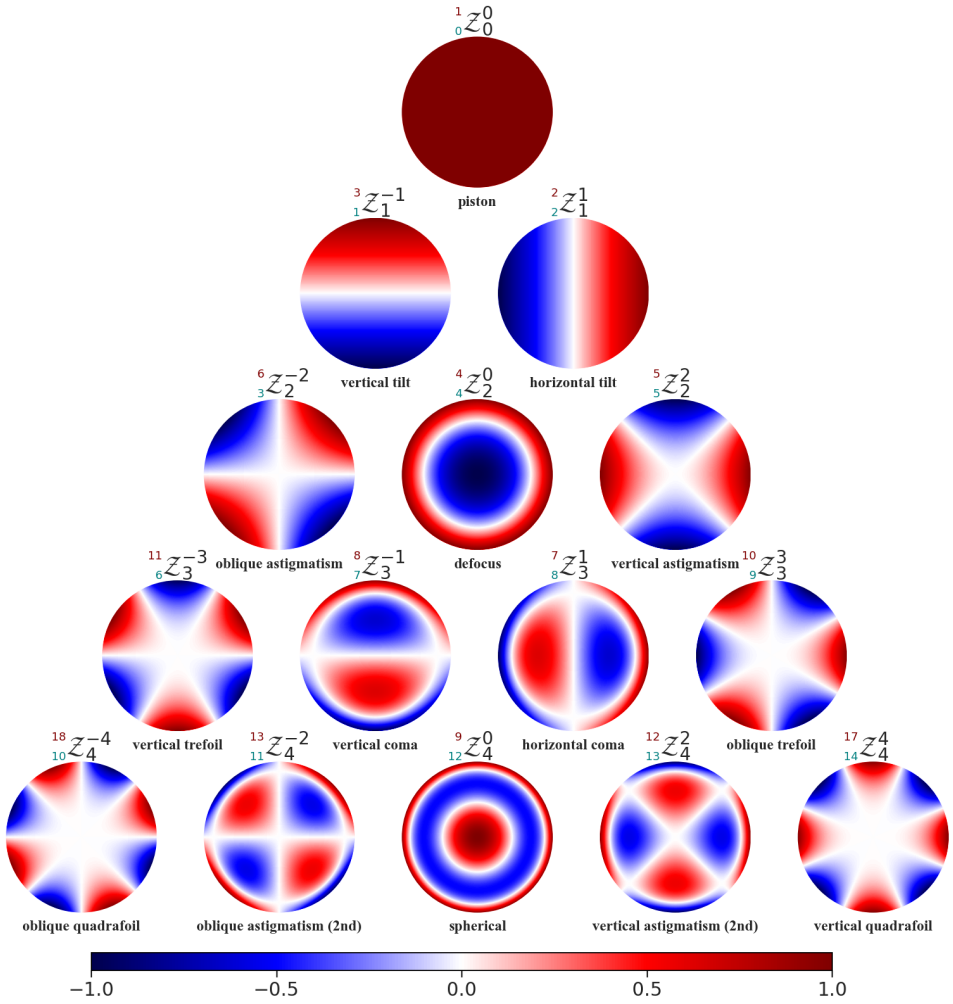

Figure 1.2: The first 15 Zernike Polynomials (ANSI ordering) plotted over the unit disc. Each disc is labeled with the aberration name (below) along with the symbol $\boxed{{}^{j_f}_{j_a}\mathcal{Z}_n^m}$ (above) where n is the radial order, m is the azimuthal order, j_f (maroon) is the Fringe Polynomial index, and j_a (teal) is the ANSI/OSA Polynomial index.

Chapter 2: Scattering Aberration Correction

2.1 Introduction

The problem of aberration correction using phase or amplitude modulating elements such as deformable mirrors or spatial light modulators (SLMs) can be separated into two main approaches. The first approach is to use the Zernike basis where a set of Zernike Polynomial functions are used as orthogonal modulation modes to overcome low order aberrations in weakly scattering media [2, 1, 19]. The second approach is to use a spatially Segmented basis where the SLM is divided into a grid of spatially independent modes to overcome aberrations from strongly scattering media (see Figure 2.1)[13].

The purpose of the experiment is to test how well aberrations due to scattering particles in biological like materials can be corrected for by finding the optimal phase shape of a laser wavefront using each of these bases. The Segmented basis has been applied to wavefront shaping in optically thick scattering media [13], but it is unclear how "thick" a material must be before the Segmented basis provides an advantage over the Zernike polynomial basis used predominantly in AO correction for optically thin media.

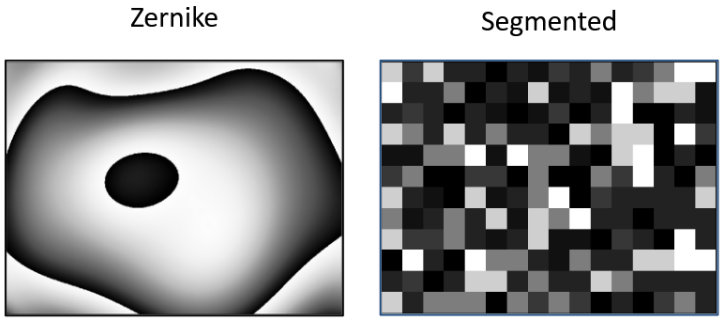

Figure 2.1: Example of random phase patterns generated by the Zernike basis and the Segmented basis over the active area of the spatial light modulator.

2.2 Materials and Methods

2.2.1 Phantom Aberration Correction Experiment

We compared the relative effectiveness of using the two bases to correct for optical aberrations in materials of varying turbidity using the optical setup in Figure 2.2. A 532 nm laser beam is linearly polarized, spatially filtered through a pinhole aperture, expanded, and reflected off of a Holoeye LC-R 2500 liquid crystal spatial light modulator (SLM). The beam is then focused with an objective lens (NA=0.4, 20x) onto a scattering sample, and a second objective (NA=0.4, 20x) imaged the focus plane within the sample. An 8-bit CCD camera (DMK21BU04, Imaging Source) collected the output intensity pattern. The SLM phase response was linearized using an interferometric method discussed in Section 2.2.5 [20].

For each sample, optimization algorithms were carried out in which the optimal phase pattern on the SLM was found for each of the bases. The optimal

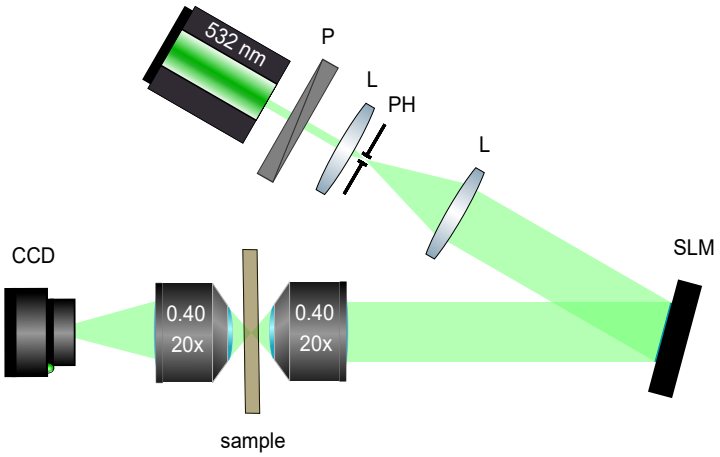

Figure 2.2: Schematic of the aberration correction optical setup. A 532 nm laser beam is expanded and reflected off of a liquid crystal spatial light modulator, with the polarization set to achieve phase-mostly modulation. The modulated beam is focused on a scattering sample, and a CCD camera measures the output intensity pattern.

phase pattern was determined to be the one that produced the highest intensity focus. The procedure for each sample went as follows: First, a Zernike polynomial optimization was executed and repeated 5 times, each time using the previous best phase mask as the starting point. The 5 optimized Zernike phase masks were then compared by taking an averaged intensity measurement over 500 frames and choosing the mask with the best focus. This repetition is necessary due to noise sensitivity in the Zernike optimization process. Second, genetic optimizations over the Segmented basis were executed with N=128 and N=512 segments, using the best Zernike phase mask as the base mask (as opposed to a uniform phase mask). To compensate for the possibility of sample optical shift between optimization runs, another Zernike optimization procedure is conducted between the N=512

and N=128 genetic optimizations, to ensure that the Zernike base mask used is optimal. Finally, genetic optimizations over the Segmented basis were executed for N=128 and N=512 segments, using a uniform phase mask as the base mask.

Due to laser intensity drift over the course of the optimization process as well as the possibility of sample optical shifts (persistence), optimized phase mask output fields could not be compared contemporaneously across all optimization runs. After each optimization, 500 focus intensity field images were collected and used to assess the focus quality with metrics (see section 2.2.4) that are insensitive to fluctuations in laser intensity.

2.2.2 Phantom Sample Preparation and Characterization

We fabricated a set of 16 scattering samples using standard optical phantom materials and design [21, 22, 23]. The samples were composed of aluminum oxide scattering particles (Al_2O_3 powder, $\leq 10\mu m$ avg. part. size, Sigma-Aldrich) embedded in a clear polyester resin (Castin' Craft Clear Polyester Casting Resin, Environmental Technology Inc.). The aluminum oxide embedded resin was cast between two microscope slides, creating an optically smooth outer surface and mitigating the need for polishing. The refractive index of the polyester (n=1.54) also closely matches that of the microscope slides (n=1.52), which leads to a low reflection interface between the two media. The set of optical phantoms had varying aluminum oxide concentration ranging from 0-45 g/L and resin thickness of 1,2, or 3 mm.

We characterized the extinction depth of each sample using a transmitted intensity measurement (see Figure 2.3), measuring a range of extinction depths between 0-8.5 after correcting for the reflection from the glass. The goal of the measurement is to determine the extinction depth τ, using the definition from the Beer-Lambert Law of the transmittance T of light passing through an attenuating medium,

$$T = \frac{\Phi_t}{\Phi_i} = e^{-\tau}, \tag{2.1}$$

where Φ_t is the transmitted flux, Φ_i is the incident flux, and τ is the optical depth the medium. Rearranging equation 2.1 as

$$\tau = -\ln T \tag{2.2}$$

allows us to determine τ directly from the measurement of the transmittance T for each sample. Importantly, since this measurement does not distinguish between absorption by the sample and scattering, we will be referring to τ simply as the extinction depth.

As an optical substrate, polyester is clear with low intrinsic absorption and scattering with a refractive index n=1.54 close to that of many tissues. Aluminum oxide scatterers in polyester have been shown to have a high anisotropy factor, meaning they exhibit forward dominant scattering [24]. The scattering material with an average particle size $\leq 10\mu m$ was chosen to match the size of common scattering structures in biological tissues and produce strong interaction with our 532 nm light source. Because the polyester substrate is optically clear, the op-

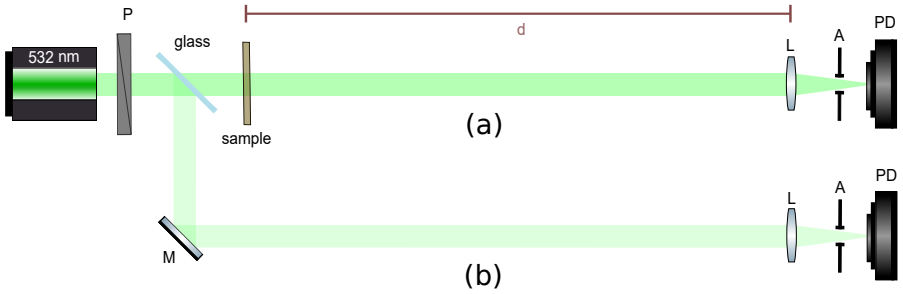

Figure 2.3: Optical set up for the phantom transmission test. A 532 nm laser beam is split into two paths (a) and (b) using a glass microscope slide. The light in path (a) passes through the sample being tested before being focused by a lens (L) through an aperture (A) onto a photodiode (PD). Reference path (b) reflects off of a mirror (M) before also being focused through an aperture onto a second PD. The voltage on each PD is read by an oscilloscope. To compensate for potential laser intensity fluctuations, the voltage measurement from the PD on reference path (b) is used to normalize the measurement from the PD on sample path (a). Distance d between the sample and the lens is large ($\approx 1m$) in order to minimize measurement of scattered light.

tical extinction of each sample can be assumed to be due almost entirely to the aluminum oxide particles.

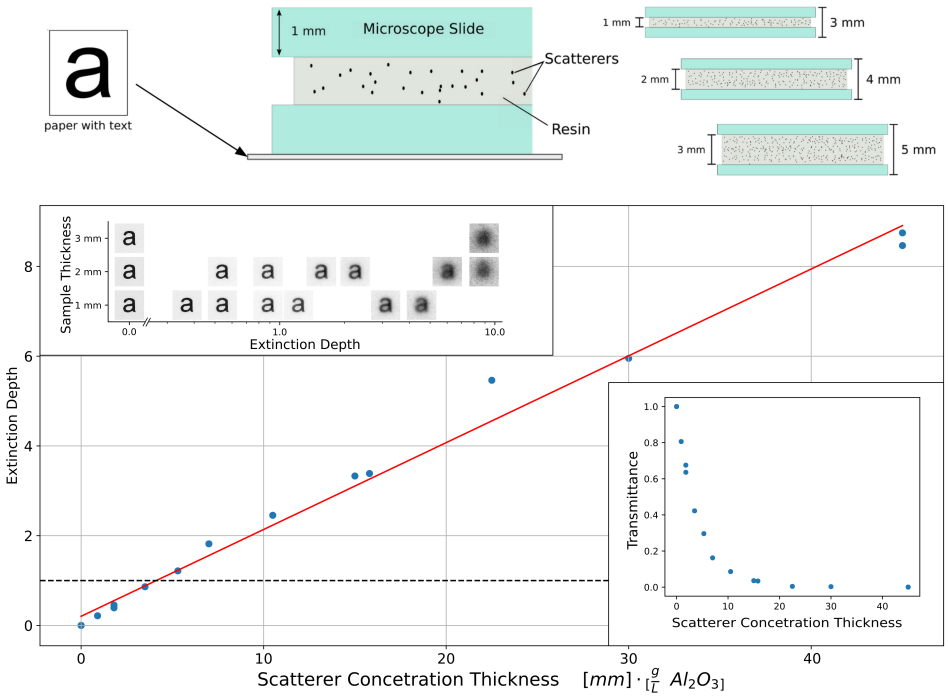

Figure 2.4: Phantom extinction depth τ vs. Scatterer Concentration Thickenss ($[mm] \cdot [\frac{g}{L} Al_2O_3]$). Extinction depth τ of the phantom samples as a function of the Scatterer Concentration Thickness calculated from the transmittance measurements. Transmittance measurements for the phantom samples as a function of the Scatterer Concentration Thickness. Optical phantom distortion of text printed on paper (12-pt Arial font). Text Imaged with microscope slide glass contacting paper surface, creating a 1 mm glass separation between text and resin surface.

2.2.3 Wavefront Optimization

The goal of optimization in this experiment is to search through the space of all possible wavefront modulation patterns to find an optimal phase pattern for correcting the imaging wavefront. Given an optical wavefront Ψ with wavelength λ propagating along the z direction,

$$\Psi = e^{ikz}, \tag{2.3}$$

where $k = \frac{2\pi}{\lambda}$, and $z = z(x, y) = z(r, \theta)$, we can decompose $\frac{z}{\lambda}$ into a sum of Zernike Polynomials,

$$W(r, \theta) = \frac{z(r, \theta)}{\lambda} = \sum_j c_j \mathcal{Z}_j(r, \theta), \tag{2.4}$$

where c_j, $\mathcal{Z}_j$, and W are dimensionless with scale λ. Therefore, if we have an ideal wavefront described by $W(r, \theta)$, then we can describe an aberrated wavefront by,

$$\Psi = e^{i2\pi(W+\Delta W)}, \tag{2.5}$$

where the term ΔW describes the aberration to the ideal wavefront, or wavefront error (see Figure 2.5). The goal of wavefront optimization, then, is to shape the incident wave such that the wavefront error is minimized.

The two bases we are comparing have different properties and require different approaches (algorithms) when it comes to wavefront optimization. To define what is optimal one needs a metric, or set of metrics, which accurately describe the relative quality of measurements. It is common to use the maximum intensity of

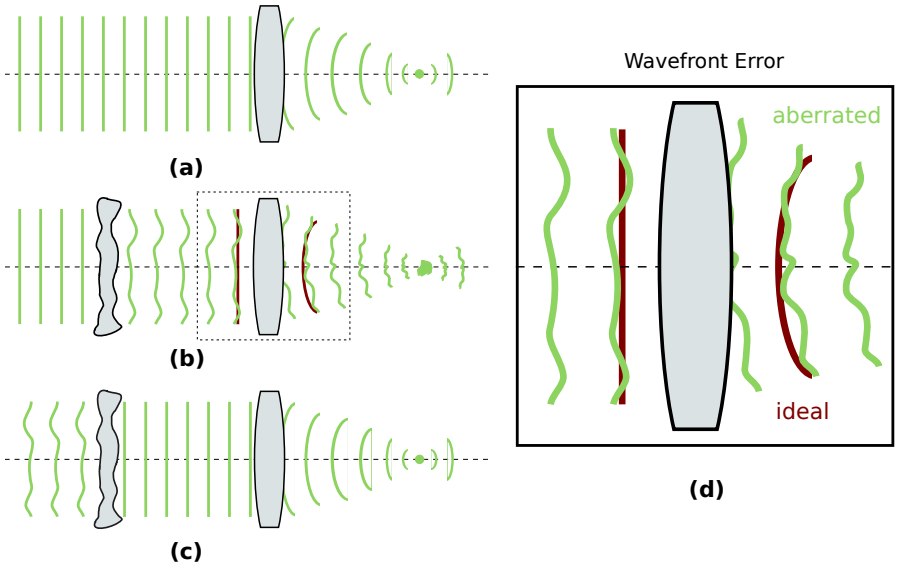

Figure 2.5: Wavefront correction and wavefront error. (a) Optically flat (ideal) plane wave focused by a lens. (b) Optically flat plane wave propagating through an aberrating medium focused by a lens. Ideal wave shown (red) for comparison. (c) Wavefront shaped such that after propagating through the aberrating medium, an ideal wavefront emerges. (d) Wavefront error visualized for (b).

the focus as a metric. However, to compensate for significant intensity noise in our light source, we instead used a weighted maximum intensity metric

$$max_w(\mathcal{I}_{ROI}) = \sum_{n=1}^{N} w_n \mathcal{I}_n^s \tag{2.6}$$

where N is the number of weights, $\mathcal{I}_{ROI}$ is the set of intensity values of the pixels in the focus region of interest (ROI), $\mathcal{I}^s$ is the set of ROI pixel intensity values sorted from highest intensity to lowest intensity, and $\mathcal{I}_n$ is the n_{th} highest pixel intensity value in the ROI. In this work, we use a ROI of 50x50 pixels defining the focus region. The weights

$$w_n = \begin{cases} 0.56 & \text{if } n = 1, \\ 0.04 & \text{if } 2 \leq n \leq 9, \\ 0.01 & \text{if } 10 \leq n \leq 21 \end{cases} \tag{2.7}$$

were chosen such that higher intensity pixels were given higher weights, the brightest pixel intensity contributes the majority of the metric value, and that $\sum_n w_n = 1$. The effect of this weighting regime is to reduce the noise sensitivity of a strict maximum intensity value, while still ranking intensity patterns that are brighter and more compact. The effect of the weighting, when applied to a focused spot, is visualized in Figure 2.6.

Other metrics have been proposed such as the S_1 spot sharpness metric [25, 26],

$$\mathcal{S} = \frac{\sum_n \mathcal{I}_n^2}{(\sum_n \mathcal{I}_n)^2} \tag{2.8}$$

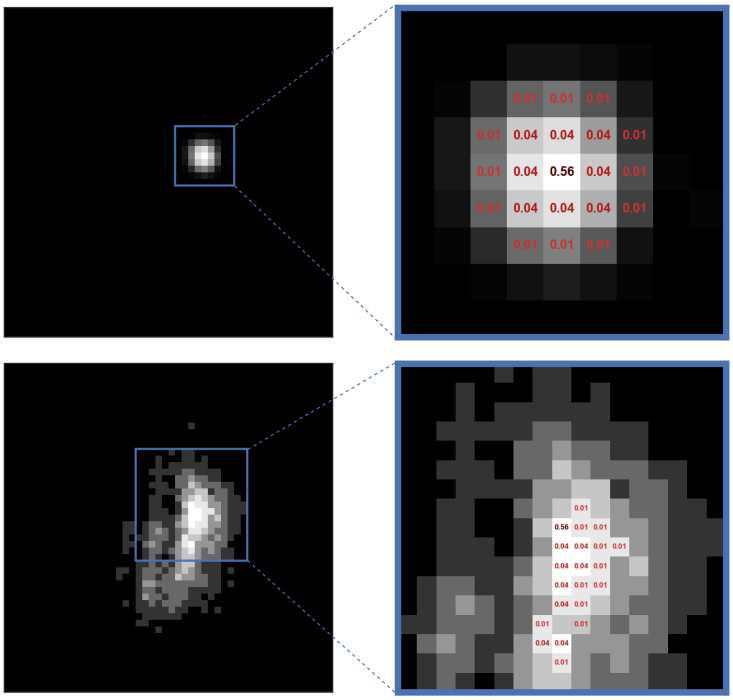

Figure 2.6: (left) Focus region of interest intensity pattern, $\mathcal{I}_{ROI}$. (right) Zoomed in view of the focus intensity pattern with weights w_n (red) shown on pixels as would be applied by the max_w function. For comparison, $max_w(\mathcal{I}_{ROI}) = 40.9$ and $max(\mathcal{I}_{ROI}) = 50$.

where $\mathcal{I}_n$ are the individual pixel intensity values in the focus ROI. However, $\mathcal{S}$ does not work as an optimization metric for the random search algorithms because it can be optimized by decreasing the number of pixels with non-zero values, which can be achieved by decreasing the average intensity of $\mathcal{I}_{ROI}$. The genetic algorithm we used for optimizing the segmented basis is a random search algorithm. For consistency, we used the max_w as the optimization metric for both the Zernike and Segmented optimization algorithms.

2.2.3.1 Zernike Optimization Algorithm

In the Zernike basis the wavefront is decomposed into a set of two dimensional polynomial functions. The number of optimization modes is defined by the number of polynomials included in the optimization. In this work, we optimize over the first 49 polynomials (see Figure 2.7), excluding the first three (piston, tip, and tilt). This gives a total of 46 optimization modes.

The optimization algorithm that we use for the Zernike basis involves taking max_w intensity measurements over a range of coefficients, creating a least-squares fit of the measurements using a parabolic function, and choosing the optimal coefficient as the one corresponding to the maximum of the parabolic fit. The parabolic function is

$$f(x) = a - b(x - x_0)^2, \tag{2.9}$$

where a, b, and x_0 are the fitted parameters, and x is the Zernike coefficient value. The Zernike optimization algorithm is described in Figure 2.8.

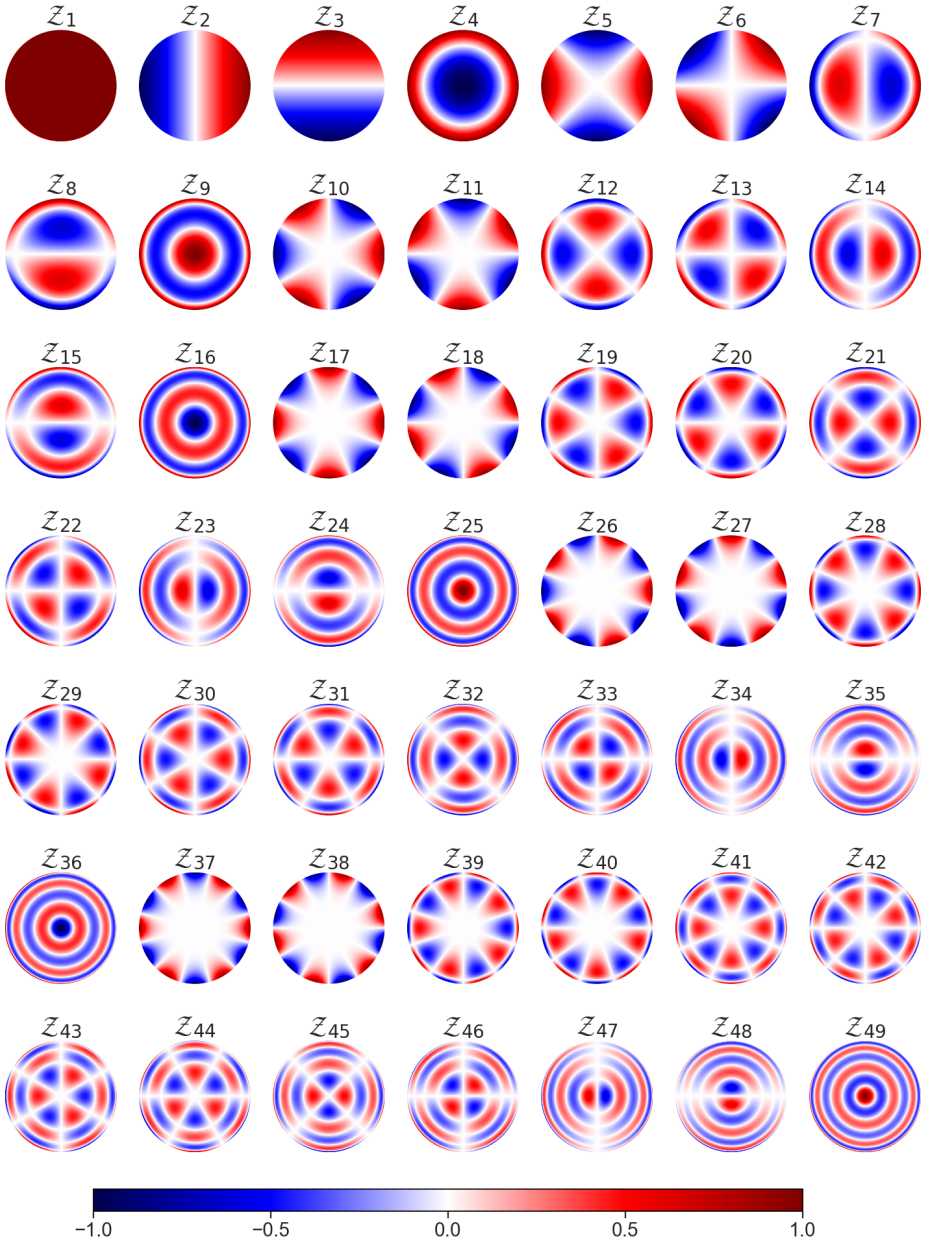

Figure 2.7: The first 49 Fringe Zernike Polynomials plotted over the unit disc. Each plot is labeled with Z_j, where j is the Fringe Polynomial index.

For each Zernike Polynomial $\mathcal{Z}_j$ being optimized:

1. *Coarse Search:*
   (a) For Zernike coefficients $c_k = 40k$, for all integers $k \in [-20, 20]$, load the Zernike mask $c_k\mathcal{Z}_j$ onto the SLM and take a measurement $max_w(\mathcal{I}_{ROI})$ of the resulting focus ROI
   (b) Create a least squares fit of data $(c_k, max_w(\mathcal{I}_{ROI}(c_k)))$ using a parabolic function $f(c_k)$ (Eq. 2.9)
   (c) Select the optimal coefficient as the one which maximizes the parabolic fit $x_{approx} = \text{argmax}(f(c_k))$
2. *Fine Search:*
   (a) For Zernike coefficients $c_k = x_{approx} - 8k$, for all integers $k \in [-10, 10]$, load the Zernike mask $c_k\mathcal{Z}_j$ onto the SLM and take a measurement $max_w(\mathcal{I}_{ROI})$ of the resulting focus ROI
   (b) Create a least squares fit of data $(c_k, max_w(\mathcal{I}_{ROI}(c_k)))$ using a parabolic function $f(c_k)$ (Eq. 2.9)
   (c) Select the optimal coefficient as the one which maximizes the parabolic fit $x_{best} = \text{argmax}(f(c_k))$

Figure 2.8: The Zernike optimization algorithm.

The algorithm takes advantage of the roughly parabolic shape of the metric function $max_w(\mathcal{I}_{ROI}(x))$ near the maximum, as is shown in Figure 2.9 for polynomials $\mathcal{Z}_4 - \mathcal{Z}_{11}$. The purpose of the "coarse search" step is to locate the approximate optimum x_{approx}. Once the approximate optimum is located the "fine search" fits the metric function near the maximum, where the data are highly parabolic in shape. Figure 2.10 shows the fine search step applied to polynomials $\mathcal{Z}_4 - \mathcal{Z}_7$ on an aberrated optical setup.

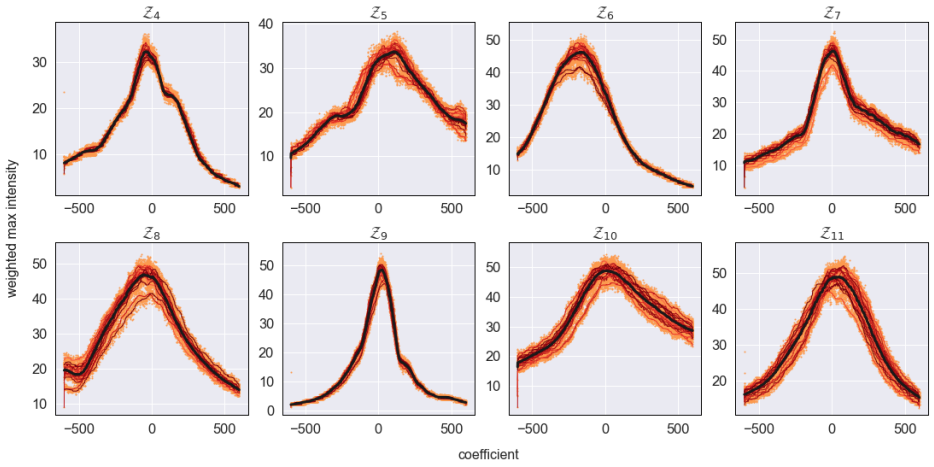

Figure 2.9: Weighted max intensity of the focus plotted as a function of the Zernike coefficient value for polynomials $Z_4 \rightarrow Z_{11}$ over 23 data collection runs on an aberrated optical setup. For each run, the weighted max intensity was recorded for each integer [-600,600]. Black line indicates the averaged value across all runs.

2.2.3.2 Segmented Optimization Algorithm

In the Segmented basis the wavefront is decomposed into spatially contiguous regions (segments) of arbitrary shape, and the number of independent optimization

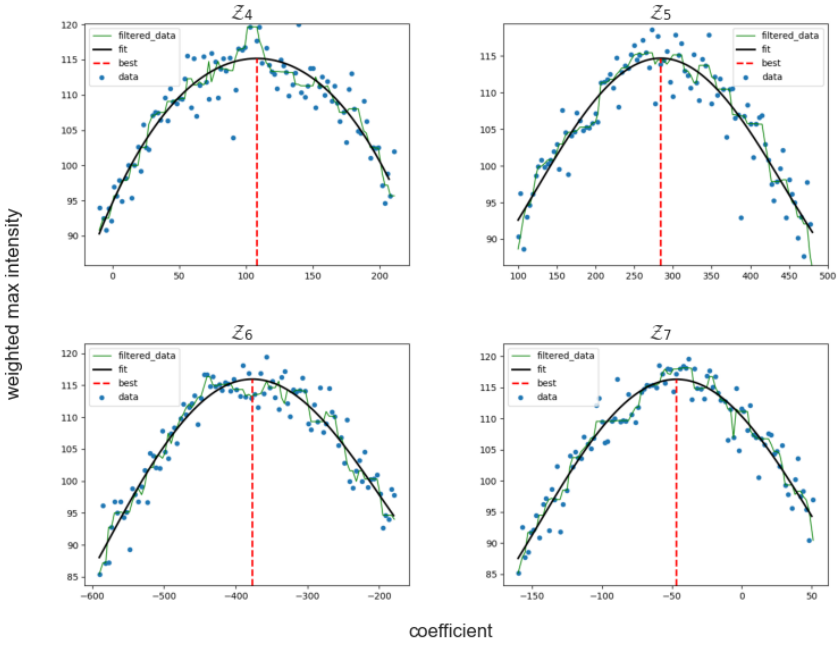

Figure 2.10: Zernike optimization data for polynomials $Z_4 \rightarrow Z_7$. Weighted max intensity measurements (blue dots) is shown as a function of coefficient value. Polynomial fit (black line) is shown along with the optimal coefficient (red dashed line) chosen from the maximum of the polynomial fit. This is the "fine search" part of the optimization process, where a narrow range of coefficients around the "coarse search" optimum are searched over to acquire a good polynomial fit.

modes is defined by the number of segments (see Figure 2.11). Unlike the Zernike basis, which is defined continuously over the unit disc, the Segmented basis is discrete by definition. Therefore, the spatial frequency of any phase pattern described in the Segmented basis is determined by the size and shape of the individual segments. Fitting high frequency aberrations requires a high number of modes to be optimized.

In this work, a rectangular segment shape is used with two different segment sizes corresponding to $N = 128$ (32x48 pixels) and $N = 512$ (64x96 pixels) optimization modes. Due to the comparatively high number of optimization modes employed when using the Segmented basis, random optimization algorithms such as Partition, Genetic, or Particle Swarm algorithms are generally more efficient than sequential optimization algorithms [27, 28, 29].

2.2.3.3 Genetic Algorithm

In this work we use a Genetic Algorithm (GA) to optimize the phase masks in the Segmented basis. The algorithm is based on the process of natural selection in biological systems, and provides an efficient and robust optimization process for high dimensional spaces. The algorithm can be broken up into the following elements:

Generate Initial Population: Generate an initial population of M_p SLM phase masks (parent masks), each with randomly chosen phase values.

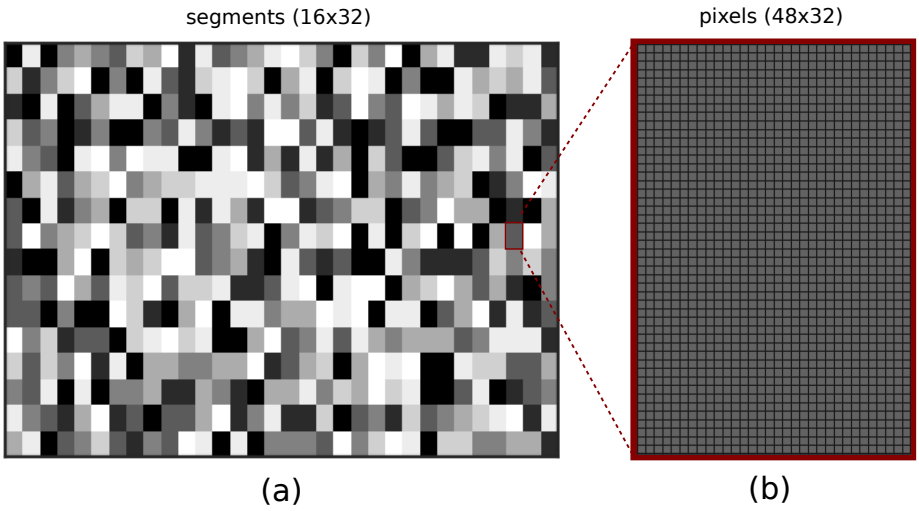

Figure 2.11: Segmented Basis displayed on SLM. (a) Example of a random phase mask displayed on a spatial light modulator (SLM) with segment size 48x32 pixels (WxH), giving an SLM segment resolution of 16x32 segments (N=512). The SLM pixel resolution is 1024x768. (b) View of single segment showing individual pixels.

Measure and Rank: Load each mask onto the SLM and measure its fitness metric. In this work we use max_w (Equation 2.6) as the fitness metric. Rank each parent mask based on its relative fitness metric value, with the highest rank given to the mask with the highest metric value.

Breed: Select two parent masks for breeding, with a higher probability of selection given to higher ranked masks. Produce a new "child" mask from the two parents by randomly generating a binary matrix T. The segments of the two parents will be combined to make the new mask according to $Child = P_1 \cdot T + P_2 \cdot (1 - T)$. Randomly choose a new phase value for (mutate) a proportion, R, of the segments of the child mask according to $R = (R_i - R_f) \cdot e^{\frac{-n}{\lambda}} + R_f$, where R_i and R_f are the initial and final mutation rates, n is the generation number, and λ is the decay factor.

Select: Keep the top M_p ranked masks from the combined population of child and parent masks, removing the M_c lowest ranked masks. This becomes the parent mask population for the next generation.

The full algorithm is described in Figure 2.12. The algorithm randomly searches the SLM phase pattern space over G generations, maximizing the value of the fitness function. In this work, we use values $M_p = 20$, $M_c = 15$, $R_i = 0.05$, $R_f = 0.001$, and $\lambda = 650$. For number of generations G we use values between $1500 - 3000$, with higher values of G used when optimizing over a higher number of optimization modes N.

1. *Generate Initial Population* of M_p parent masks
2. For each generation in G total generations:
   (a) *Measure and Rank* the parent masks
   (b) *Breed* M_c new child masks
   (c) *Measure and Rank* the child masks
   (d) *Select* the best M_p masks from the combined population of parent and child masks
3. Select highest ranked mask in the final population as the best mask

Figure 2.12: The full Genetic Algorithm.

2.2.4 Assessing Focus Quality

A separate set of metrics is used to assess the quality of the corrected image after optimization. Due to the potential for optical shifts within the samples and intensity drift in the laser light source, a simple comparison of maximum intensity or spot metric would yield biased results. Instead, we use the Full Width Half Maximum (FWHM) of the focused spot and the signal to background ratio (SBR) of the focus ROI. These metrics are more robust to the types of noise present in our optical system.

To calculate the FWHM of our focused spot, we first fit the focus intensity profile with a two dimensional elliptical gaussian function with translational and rotational freedom (see Figure 2.13 a-c),

$$g(x, y, ...) = I_0 + Ie^{-\frac{((x-x_0)\cos\theta-(y-y_0)\sin\theta)^2}{2\sigma_x^2}-\frac{((x-x_0)\sin\theta+(y-y_0)\cos\theta)^2}{2\sigma_y^2}}, \tag{2.10}$$

where the parameters $I_0, I, x_0, y_0, \sigma_x, \sigma_y, \theta$ are fit using a least squares method. Once the parameters are fit, we compute an averaged FWHM value,

$$\overline{\text{FWHM}} = \sqrt{\ln 2}(\sigma_x + \sigma_y), \tag{2.11}$$

where the un-averaged FWHM $= 2\sqrt{\ln 2}\sigma$. Given that the diffraction limited focus has a gaussian intensity profile and that the signal is strong enough to produce a good fit, the FWHM metric will be independent of the intensity, I.

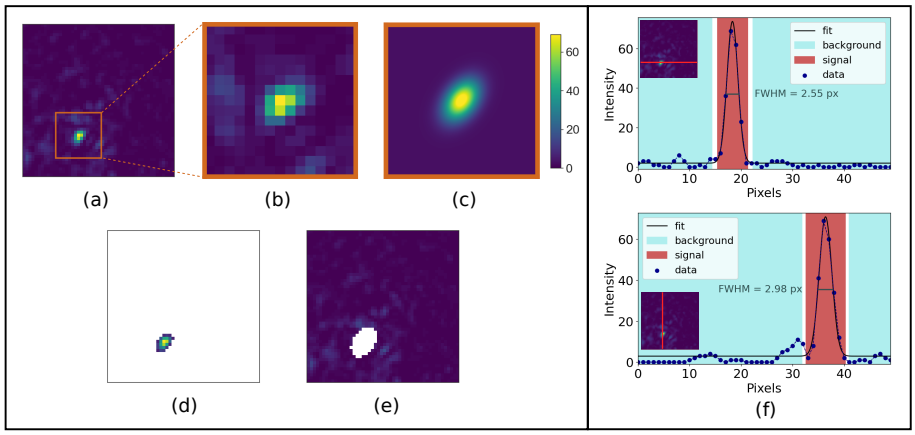

Figure 2.13: FWHM and SBR metrics. (a) Focus intensity pattern in the region of interest (ROI). (b) Zoomed in view of focus within ROI. (c) Gaussian fit of focus plotted over zoomed in view. (d) Pixels in ROI corresponding to the signal I_{sig}. (e) Pixels in the ROI corresponding to the background I_b. (f) Horizontal (top) and Vertical (bottom) pixel intensity profile plots along lines intersecting the focus maximum intensity, along with the corresponding fitted gaussian profiles. Signal pixels I_{sig} shaded with red background. Background pixels I_b shaded with blue background.

The signal to background ratio (SBR) takes into account both the amount of light in the focus and the amount of light remaining unfocused. It is especially

useful for characterizing the focus for stronger aberrations, where there remains a significant amount of unfocused light within the defined ROI after optimization. In general the SBR is calculated by taking the sum of the light in the "focused" region and dividing it by the light in the "unfocused" region of the ROI. To define "focused" and "unfocused", we use the fitted gaussian g of the focus intensity profile (Equation 2.10). Given the fitted intensity values of $g(x, y)$ defined over the ROI region,

$$SBR = \frac{\sum_s I_{sig}}{\sum_b I_b}, \tag{2.12}$$

where pixels I_{sig} are the ROI pixels where $g(x, y) > 0.05I + I_0$, and pixels I_b are the ROI pixels where $g < 0.001I + I_0$. In other words, the signal is the ROI region corresponding to 5% of the gaussian fit maximum intensity and above. The background is the ROI region corresponding to 0.1% of the gaussian fit maximum intensity and below. Given Equation 2.10, intensity thresholds 0.05 and 0.001 correspond to a distance from the focus center of 2.45σ and 3.72σ, respectively. The performance of the SBR metric on unfocused and focused ROIs is shown in Figure 2.13.

2.2.5 SLM Calibration

We calibrated the SLM using an interferometric method [20] in order to ensure a linear phase response. The method relies on measuring the interference pattern of a collimated laser beam reflecting off of the SLM with a pattern consisting of a binary grating on one half and a uniform piston on the other half as shown in

Figure 2.14.

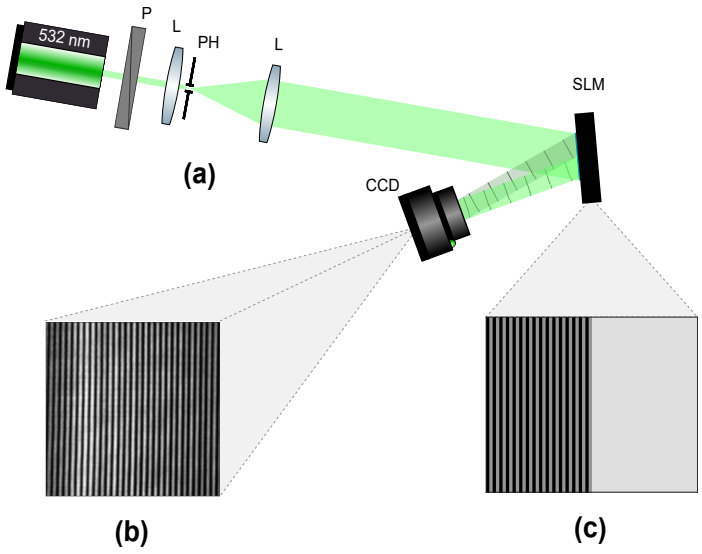

Figure 2.14: Optical set up for spatial light modulator (SLM) phase calibration experiment. (a) A 532 nm laser beam is filtered and expanded before being reflected off of a liquid crystal SLM. An interference pattern is collected by an 8-bit CCD camera (DMK21BU04). (b) Example interference pattern. (c) Example of SLM phase pattern. The left half of the SLM displays a binary grating pattern, and the right half of the SLM displays a uniform piston pattern. The binary grating is kept fixed, while the pixel grey value of the piston pattern is incrementally adjusted. The resulting interference pattern, created by the tilted first diffraction order reflecting off of the binary grating overlapping with the un-tilted wavefront reflecting off of the piston region, is measured to determine the corresponding phase shift.

The first diffraction order from the portion of the wavefront that reflects off the binary grating forms a tilted plane that interferes with the un-tilted wavefront reflecting off the piston, creating the interference pattern seen in Figure 2.14 (b) on the CCD camera (DMK21BU04, Imaging Source). For each piston grey value g, an interference pattern image was collected, filtered, and averaged along the

axis parallel to the fringes to produce a fringe profile (Figure 2.15).

The equation describing the interference fringe profile produced by a collimated beam reflecting off of binary phase grating adjacent to a uniform piston phase pattern is,

$$I(x, g) = I_0 + \Delta I \cdot \cos\left(2\pi x/P + \phi_0 + \Delta\phi(g)\right), \tag{2.13}$$

where I_0 is the background intensity, ΔI is the interference fringe amplitude, P is the fringe period, x is the pixel distance, $\Delta\phi$ is the phase shift term, and g is the piston grey value. What we're really interested is in the interference term,

$$I(x, g) - I_0 = \Delta I \cdot \cos\left(2\pi x/P + \Delta\phi(g)\right). \tag{2.14}$$

This allows us to directly measure the phase shift $\Delta\phi(g)$ as a function of the pixel grey value, g, in the piston half of the SLM.

We use the Discrete Fourier Transform (DFT) to retrieve phase information using the shift theorem from the fringe intensity profiles. This produces sub-pixel resolution measurement of spatial shift, and is more accurate than a direct space domain measurement. The shift theorem states that a Δx shift in a signal's space (or time) domain corresponds to a linear phase shift term, $\Delta\phi$, in the frequency domain.

$$\mathcal{F}\left[f\left(x - \Delta x\right)\right](\omega_k) = e^{-i\omega_k \Delta x}\mathcal{F}\left[f\left(x\right)\right](\omega_k), \tag{2.15}$$

where $\mathcal{F}$ is the Fourier Transform function, f is a spatial signal function, $\omega_k = 2\pi\frac{k}{N}$ $\frac{rad}{N\,samples}$, N is the number of samples, and $k, \Delta x \in \{1, 2, 3, ..., N\}$.

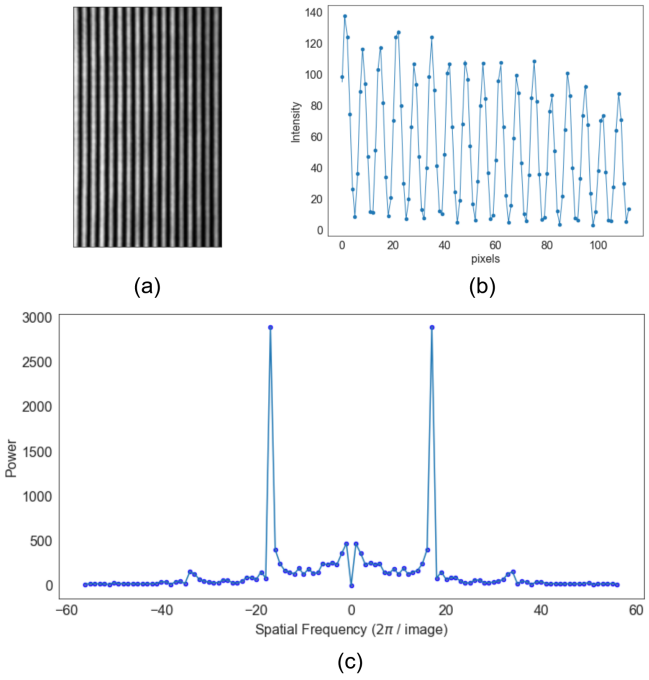

Figure 2.15: Example of data from calibration experiment. (a) Raw image, (b) fringe profile, and (c) DFT of fringe profile.

Since the spatial shift in fringe pattern adds a linear phase term in the frequency domain, then the phase at a particular frequency ω_k will be given by

$$\phi_k(g) = \phi_{0,k} + \Delta\phi_k(g), \tag{2.16}$$

where $\phi_{0,k} = \phi_k(0)$ (zero-shift phase) and $\Delta\phi_k(g) = \omega_k \Delta x(g)$. The frequency ω_k that we want to measure is the base frequency of the fringe profile, easily identified in the power spectrum. Therefore, given the complex DFT coefficient

$$\mathbf{x}_k = \sum_{n=0}^{N-1} x_n \cdot e^{-i\omega_k n} = a_k + ib_k, \tag{2.17}$$

one can extract the phase value as follows,

$$\phi_k = \tan^{-1}\left(\frac{Im(\mathbf{x}_k)}{Re(\mathbf{x}_k)}\right) = \tan^{-1}\left(\frac{b_k}{a_k}\right) \tag{2.18}$$

Inserting this into equation 2.16 and rearranging, we get

$$\Delta\phi_k(g) = \tan^{-1}\left(\frac{b_k(g)}{a_k(g)}\right) - \phi_{0,k}. \tag{2.19}$$

Applying this to our fringe profile measurements, we calculated the relative phase shift $\Delta\phi$ for each g (see Figure 2.16, top panel). From this data, we generated a look up table (LUT) which maps each "uncorrected" pixel value to the "corrected" pixel value corresponding to a linear phase shift (see Figure 2.16, bottom panel). To account for measurement noise, we calculated a least squares fit of the uncorrected

phase measurements with a polynomial function (degree 8). The fitted polynomial function was then used to generate the LUT mapping of $g_{uncorrected} \rightarrow g_{corrected}$.

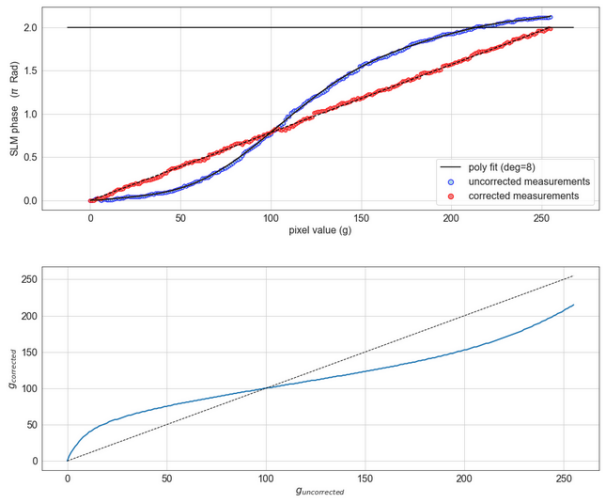

Figure 2.16: SLM calibration curves. (top) Measurements of $\Delta\phi(g)$ for the uncorrected SLM and the corrected SLM. A polynomial fit of the uncorrected phase measurements was used to produce the look up table. (bottom) Look up table created to linearize the phase response of the SLM pixels as a function of the pixel grey value g.

Once the corrected set of pixel values were found, we collected a second set of phase measurements using the corrected pixel values, which showed a highly linear phase response (see Figure 2.16, top panel). The successful calibration can also be seen in the set of fringe patterns displayed in Figure 2.17, which shows the phase error (equation 2.20) at values of g corresponding to target phase shift values $\phi_{target} = 0, \frac{\pi}{2}, \pi, \frac{3\pi}{2}, 2\pi$.

$$\phi_{error}(g) = \phi_{measured}(g) - \phi_{target}(g). \tag{2.20}$$

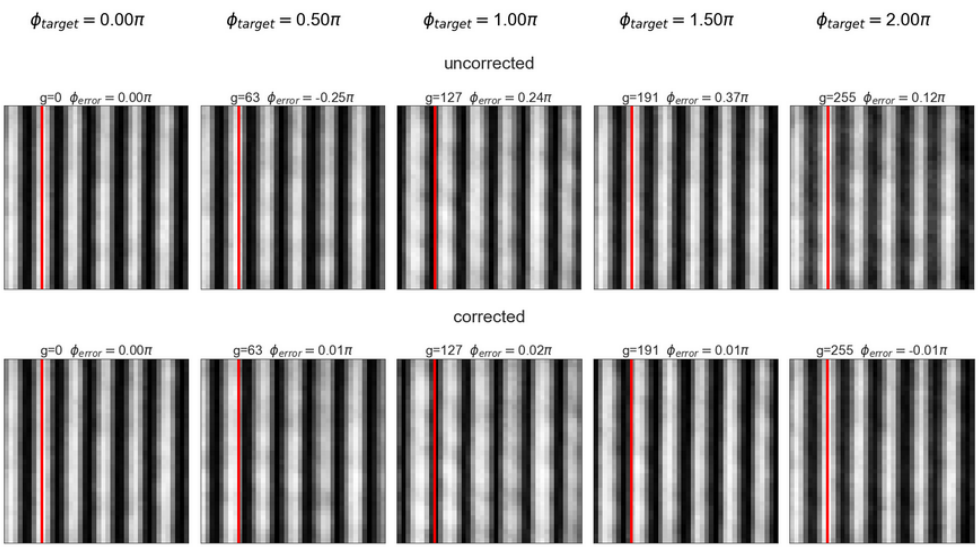

Figure 2.17: Experimental fringe patterns for the uncorrected and corrected measurements at various grey values along with the corresponding phase error compared to the ϕ_{target} of a perfectly linearized phase response.

2.3 Results and Discussion

After running the aberration correction experiment described in Section 2.2.1 on the set of phantom samples, we characterized the focus of the 500 optimized focus intensity field images. The focus quality was assessed using the Full Width Half Maximum (FWHM) and signal to background ratio (SBR), described in Section 2.2.4. The number of optimization sets for each sample Extinction depth is shown in Figure 2.18 (c). For each optimization set, there are six different individual optimizations as described in Table 2.1.

In Figure 2.19, the optimized focus intensity fields and optimized masks are shown for the N=512 optimizations on a sample with $\tau = 2.2$. The baseline (no correction) focus pattern is also shown, which helps to visualize the relative

Optimization	Description
Zernike N=512	*Zernike basis optimization over $\mathcal{Z}_4 - \mathcal{Z}_{49}$. Also used for the Zernike-Segmented N=512 optimization.*
Zernike N=128	*Zernike basis optimization over $\mathcal{Z}_4 - \mathcal{Z}_{49}$. Also used for the Zernike-Segmented N=128 optimization.*
Zernike-Segmented N=512	*Zernike basis optimization over $\mathcal{Z}_4 - \mathcal{Z}_{49}$ followed by a Segmented basis optimization with N=512 optimization modes.*
Zernike-Segmented N=128	*Zernike basis optimization over $\mathcal{Z}_4 - \mathcal{Z}_{49}$ followed by a Segmented basis optimization with N=128 optimization modes.*
Segmented N=512	*Segmented basis optimization with N=512 optimization modes.*
Segmented N=128	*Segmented basis optimization with N=128 optimization modes.*

Table 2.1: Table describing the six different optimizations performed for each sample run.

improvement of the various optimization processes.

The averaged SBR and FWHM metrics as a function of extinction depth are shown in Figure 2.18 (a-b). In these plots, we see that all optimization types exhibit a decreasing SBR as τ increases. Counter-intuitively, there appears to be a slight improvement in the FWHM as τ increased. This effect has been noted by others [12], showing that wavefront shaping in scattering media can achieve sub-diffraction focusing. However, the effect is not very clear in our data, and may simply be due to varying conditions between optimization runs. In both plots, there appears to be a clear improvement of the Segmented optimizations over the Zernike-only optimizations. To illustrate this trend more clearly, we plotted the focus quality metrics for the Segmented and Zernike-Segmented optimizations normalized by the corresponding Zernike-only optimization. For both metrics, the Zernike normalized value is calculated by taking the metric value and dividing it by the metric value of the Zernike-only optimization labeled with the same number of Segmented modes N.

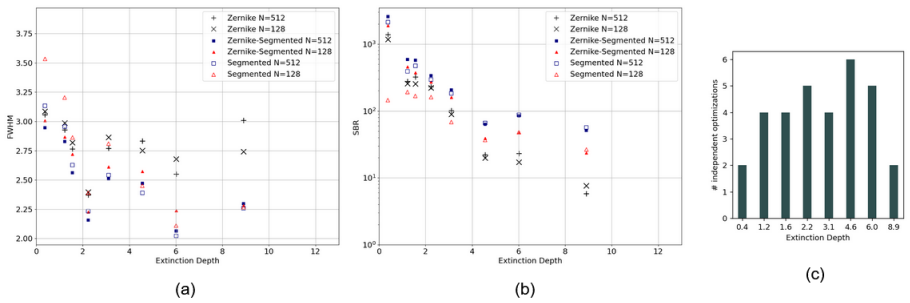

Figure 2.18: Results of phantom aberration correction experiment. (a) Average value of the Full Width Half Maximum metric as a function of the extinction depth for all optimization runs. (b) Average value of the Signal to Background Ratio metric as a function of the extinction depth for all optimization runs. (c) The number of independent optimization sets completed at each extinction depth. Each optimization set includes the six optimization types from Table 2.1.

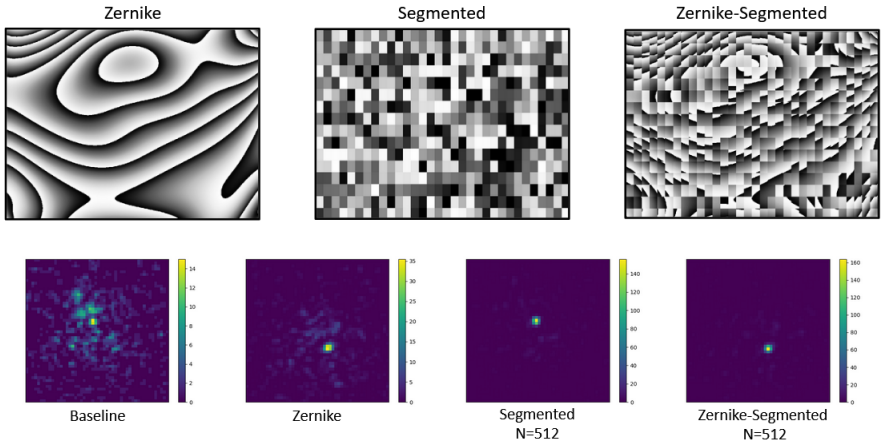

Figure 2.19: Optimized phase modulation masks and focus intensity fields. Optimized phase masks are shown for the Zernike, Segmented, and Zernike-Segmented optimizations (N=512). Focus intensity fields are shown for each of the optimized masks, alongside the Baseline (no correction) intensity pattern. Sample extinction depth $\tau = 2.2$.

The Zernike normalized SBR is shown in Figure 2.20 (a-c), and the Zernike normalized FWHM is shown in Figure 2.21 (a-c). In plots (a) the averaged values are shown. In box and whisker plots (b) and (c), the distribution of the data is shown at each optical depth.

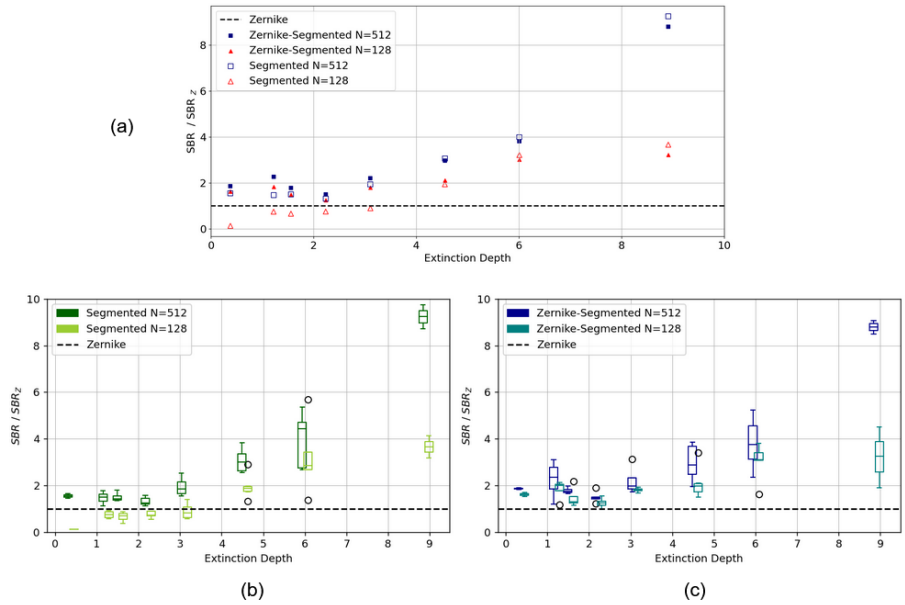

Figure 2.20: Signal to Background Ratio (SBR) of the optimized focus, normalized by the SBR value of the corresponding Zernike-only optimization, as a function of the extinction depth for all optimization runs. (a) The normalized SBR value averaged for each extinction depth. (b-c) Box and whisker plots showing the distribution of the normalized SBR metrics as a function of extinction depth for (b) the Segmented basis optimizations and (c) the Zernike-Segmented basis optimizations. *note: Boxes display median (middle box line), first quartile and third quartile (top and bottom box lines), minimum and maximum values (whiskers), and outliers (black circles). Outliers are defined by a distance greater than* $1.5(Q_3 - Q_1)$ *from the edges of the box.*

The trend of improvement of the Segmented basis optimizations over the Zernike only optimizations as τ increases can clearly be seen. In both figures there appears

to be a threshold around $\tau = 3$ where the improvement of the Segmented basis over the Zernike basis optimizations appears to steadily increase as τ increases. Below that threshold, the Zernike basis corrects for the aberrations equally well or better. Note that we would expect the Zernike-Segmented basis to always outperform the Zernike-only basis, since the Zernike-only optimized mask is the starting point for the Segmented basis optimization. Also, the Segmented basis optimizations with N=512 modes appear to be consistently better than those with N=128 optimization modes. This too we would expect, given the ability of the basis to fit higher spatial frequency aberration patterns with a higher number of modes (smaller segments). Surprisingly, the Segmented basis with N=512 optimization modes was as or more effective as the Zernike basis across the full range of samples. Previously, the Segmented basis was considered more effective at optical depths of $\tau >> 1$.

2.4 Conclusion

In this work, we explored the effectiveness of optical aberration correction over a wide range of optical depths using the Segmented and Zernike Polynomial bases. In order to do so, we first manufactured a set of 16 optical phantom samples consisting of a clear polyester resin substrate embedded with varying concentrations of aluminum oxide (Al_2O_3) scattering particles (see Section 2.2.2). We measured the scattering dominated optical depth of the sample set using a transmitted intensity experiment, recording a range $\tau = 0 - 8.5$ (see Section 2.2.2).

To test the optimization performance of each of the two optimization bases over

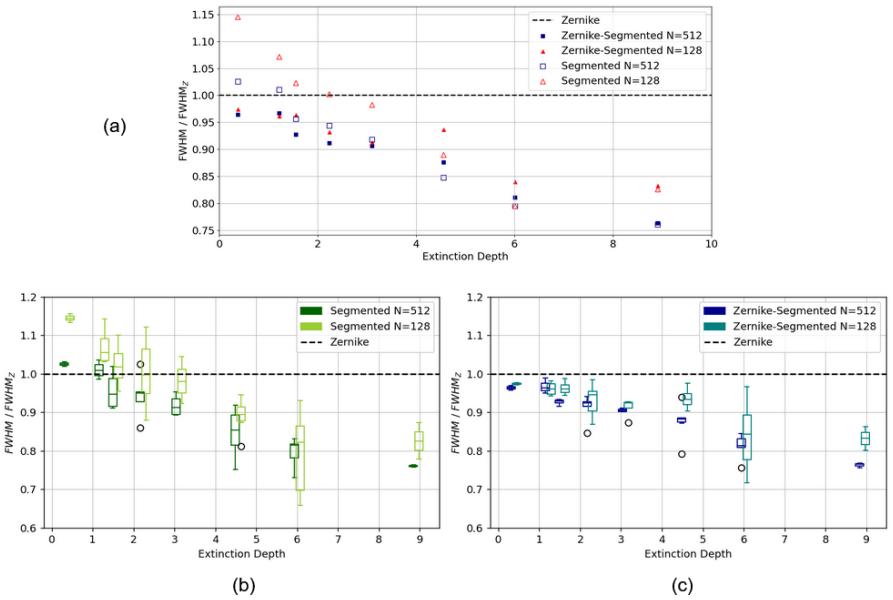

Figure 2.21: Full Width Half Maximum (FWHM) of the optimized focus, normalized by the FWHM value of the corresponding Zernike-only optimization, as a function of the extinction depth for all optimization runs. (a) The normalized FWHM value averaged for each extinction depth. (b-c) Box and whisker plots showing the distribution of the normalized FWHM metrics as a function of extinction depth for (b) the Segmented basis optimizations and (c) the Zernike-Segmented basis optimizations. *note: Boxes display median (middle box line), first quartile and third quartile (top and bottom box lines), minimum and maximum values (whiskers), and outliers (black circles). Outliers are defined by a distance greater than* $1.5(Q_3 - Q_1)$ *from the edges of the box.*

the sample set (see Section 2.2.1), we used an optical setup (Figure 2.2) in which a collimated laser beam modulated by a liquid crystal spatial light modulator (SLM) is focused within the sample before being imaged onto a CCD sensor. The goal of the experiment was to determine the range of optical depths over which each optimization basis was effective. We completed wavefront optimizations for each of the samples in the Zernike basis, the Segmented basis, and the Zernike-Segmented basis (see Section 2.2.3). The results (Section 2.3) showed that the Zernike basis was more effective at low optical depths ($\tau < 1.5$), and the Segmented bases was more effective at higher optical depths $\tau > 3$ (see Figure **??**). Surprisingly, the Segmented basis with N=512 optimization modes proved to be as or more effective as the Zernike basis across the full range of optical depths tested in this work.

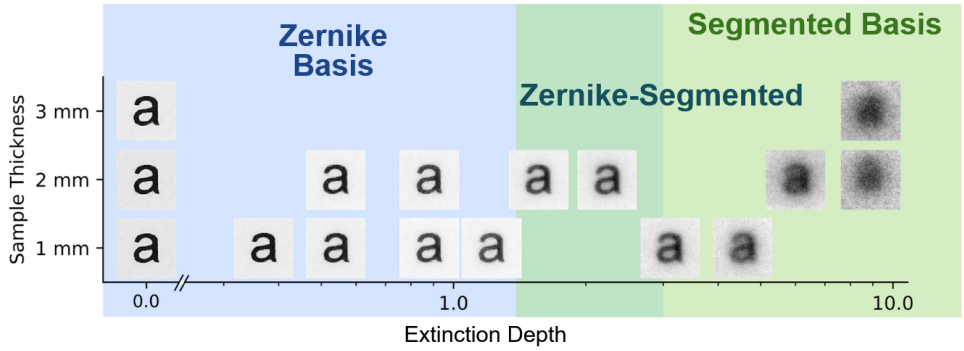

Figure 2.22: Range of effectiveness visualized for the Zernike, Zernike-Segmented, and Segmented correction bases based on our results.

These results help clarify the previously undefined overlap between the optical domains of these two commonly used optical correction bases. Hopefully, this work will be useful for those exploring new applications of Adaptive Optics and

Wavefront Shaping techniques. Future work should expand on the set of Zernike Polynomials used here. Increasing Zernike optimization to include even higher spatial frequency polynomials may show a significant improvement over the performance we showed with $\mathcal{Z}_4 - \mathcal{Z}_{49}$.

Chapter 3: NN Zernike Aberration Correction

3.1 Introduction

Optical aberrations are present in almost all imaging systems, and at a time when the fields of scientific and medical imaging are pushing the limits of diffraction in their attempts to resolve ever smaller structures and ever shorter time scales, it has become increasingly important to find improved methods for aberration correction. The field devoted to the correction of such aberrations, referred to as Adaptive Optics (AO), emerged out of the need for astronomers to correct for atmospheric aberrations in order to image further into space [1, 30, 31].

Previous work has been done applying Deep Learning (DL) algorithms to biological AO systems using Zernike polynomials [15, 16, 17, 18]. The approach taken by these groups has been to train a convolutional neural network (CNN) to take an aberrated image as input, and output the coefficients for a set of Zernike polynomials that will correct for that aberration when loaded onto an active optical element. The system being corrected is typically a coherent laser wavefront reflecting off of an SLM and focused to a point at the image plane. The input image to the network is the aberrated focus intensity pattern, typically collected by a camera sensor. Although some groups have applied this technique to systems that incorporate a direct wavefront sensor, such as a Shack Hartman Wavefront Sensor

(SHWS) [32, 33], one of the promises of the deep learning approach is to enable a simple CCD or CMOS sensor to provide the same functionality while lowering the cost and technical complexity [18].

The CNN model can be trained using a dataset generated by loading a set of Zernike polynomials with randomly selected coefficients onto the SLM, creating an aberrated image with a known correction. This process is repeated thousands or millions of times to generate a dataset which can be used to train a predictive model. Testing can be done with unseen simulated data or with aberrating materials such as biological tissue samples or optical phantoms.

3.1.1 Our Approach

In this work, we used an 18-layer ResNet architecture, pretrained on the ImageNet dataset. We applied transfer learning, re-training the model with 8M examples of aberrated images (see Section 3.2.2).

We use the Fringe Zernike Polynomial indexing, as shown in Figure 3.1. Some previous groups have also chosen not to include the tip and tilt Zernike polynomials in their model prediction, but to correct for them using a separate algorithm. These polynomials correspond to vertical and horizontal translation of the focus intensity pattern, and we think their inclusion is important to the ability of the network to predict the other polynomials accurately. So in this work we will include tip and tilt aberrations in our predictive model.

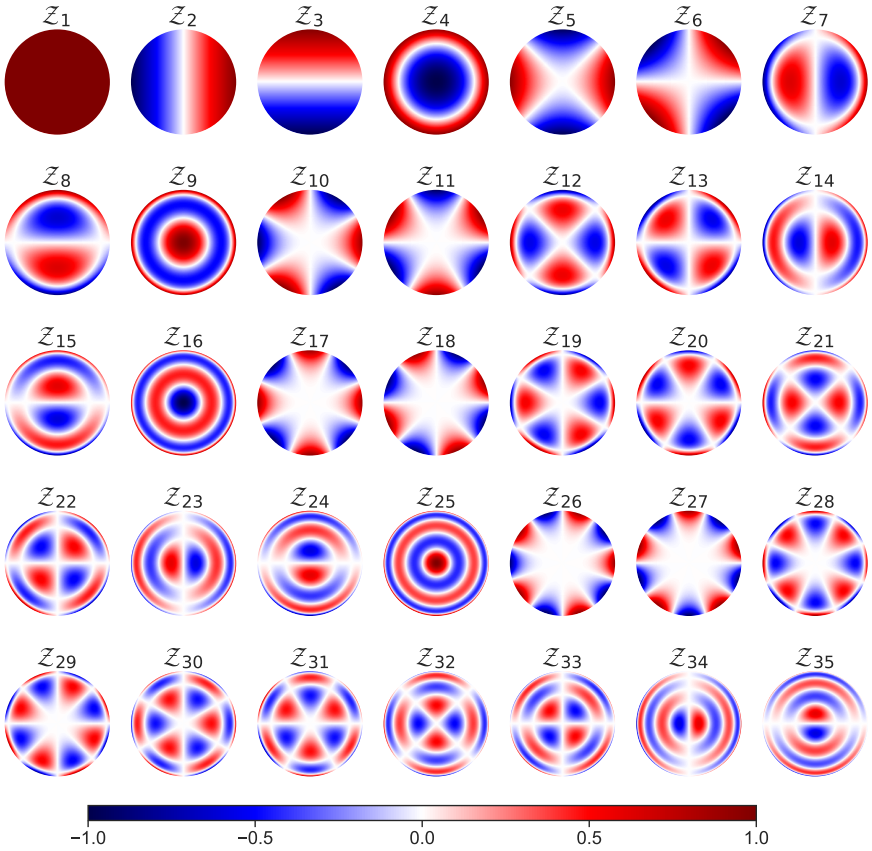

Figure 3.1: The first 35 Fringe Zernike Polynomials plotted over the unit disc. Each plot is labeled with Z_j, where j is the Fringe Polynomial index.

3.2 Methods

The experimental setup is shown in Figure 3.3. A 532 nm laser beam is linearly polarized and spatially filtered through a pinhole aperture, expanded, and reflected off of a Holoeye LC-R 2500 liquid crystal spatial light modulator (SLM). The beam is then focused onto an 8-bit CCD camera (DMK21BU04, Imaging Source), which collects the focus intensity pattern. The SLM phase response was linearized using an interferometric method discussed in Section 2.2.5 [20].

3.2.1 Training Dataset

We used the SLM to generate a dataset of eight million examples of simulated aberrations by randomly selecting coefficients for Fringe Zernike Polynomials $\mathcal{Z}_2 - \mathcal{Z}_{35}$ (see Figure 3.1). Each example consists of a set of coefficients and an aberrated image (see Figure 3.2). The coefficient range was [-0.5,0.5] (λ scale) for each polynomial. We split the dataset into 90% training set and 10% validation set.

3.2.2 Model and Parameters

The model we chose was an 18 layer ResNet architecture available through the PyTorch model library, pretrained on the ImageNet dataset. We applied transfer learning, re-training the model with 8M examples of aberrated images. We decreased some of the convolutional layer striding in order to preserve more of the spatial information before the fully connected (FC) output layer (see Figure 3.5).

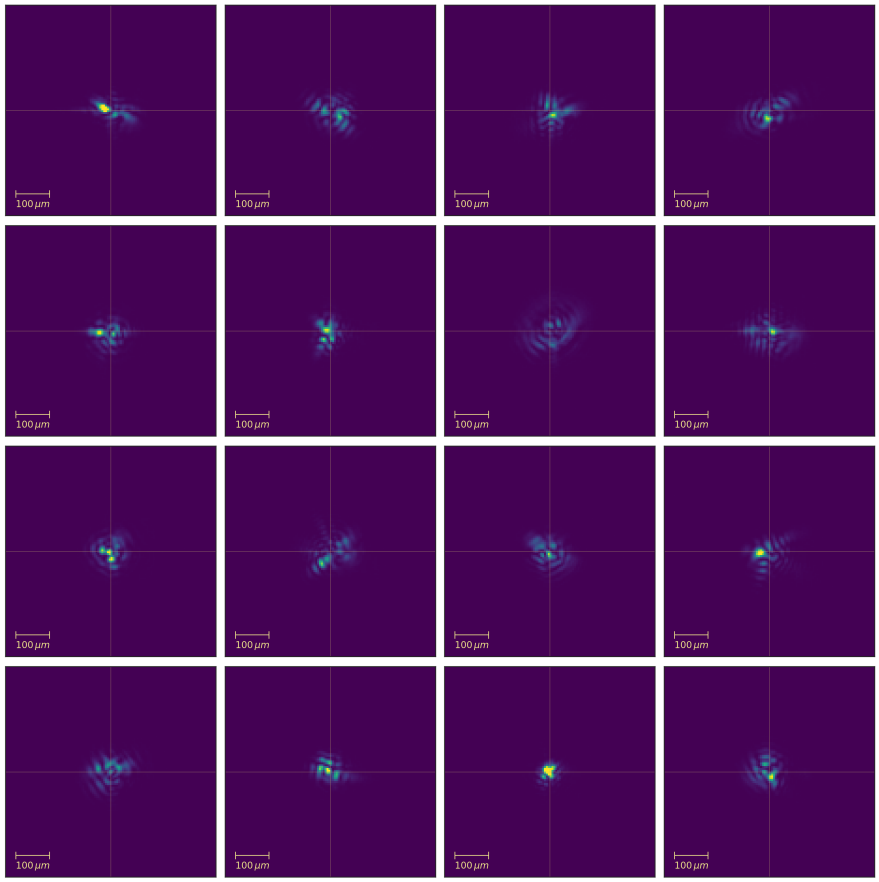

Figure 3.2: Examples of aberrated images from randomly generated Zernike Polynomials in training dataset.

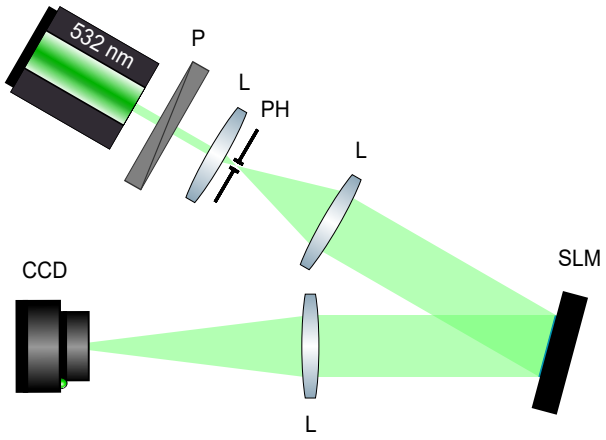

Figure 3.3: Schematic of the Deep Learning aberration correction optical setup. A 532 nm laser beam is expanded and reflected off of a liquid crystal spatial light modulator, with the polarization set to achieve phase-mostly modulation. The modulated beam is focused on a CCD camera, which measures the focus intensity pattern. Lens placed halfway between SLM and Camera, one focal length f from each.

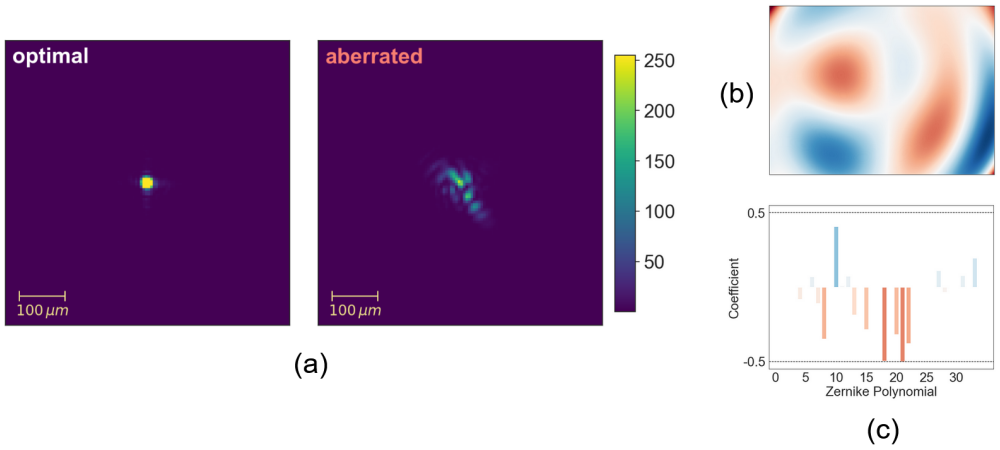

Figure 3.4: (a) Unaberrated and unaberrated focus shown for example from training dataset. (b) The SLM phase mask is shown along with (c) the Zernike Polynomial coefficients.

The layer before the FC layer outputs a $batch \times 512 \times 7 \times 7$ tensor. The goal of this modification is to increase the spatial information in the lower layers, thus improving the prediction.

The input was a 112x112 greyscale image, and the output was an 34x1 coefficient vector corresponding to the $\mathcal{Z}_2 - \mathcal{Z}_{35}$ Zernike polynomials. Before being input into the model, the image is upsampled to 336x336 using bilinear interpolation. This is done to better match the image feature scale of the ImageNet dataset. We used mean squared error (MSE) loss to optimize the network over the training dataset.

3.2.3 Image Correction Metrics

In order to assess the performance of the model in correcting for aberrations we need a set of metrics for determining the quality of the focused image. Due to the rapid timescale of correction and low order nature of the aberrations, we have chosen to use the S_1 spot sharpness metric described in [34, 25], defined as

$$\mathcal{S} = \frac{\sum_n \mathcal{I}_n^2}{(\sum_n \mathcal{I}_n)^2}. \tag{3.1}$$

As shown in Figure 3.6, a lower spot metric value generally corresponds to a more highly aberrated focus [1]. For simulated aberrations with known Zernike

[1]Spot Metric displayed in figures is scaled by 10^4 for ease of interpretation.

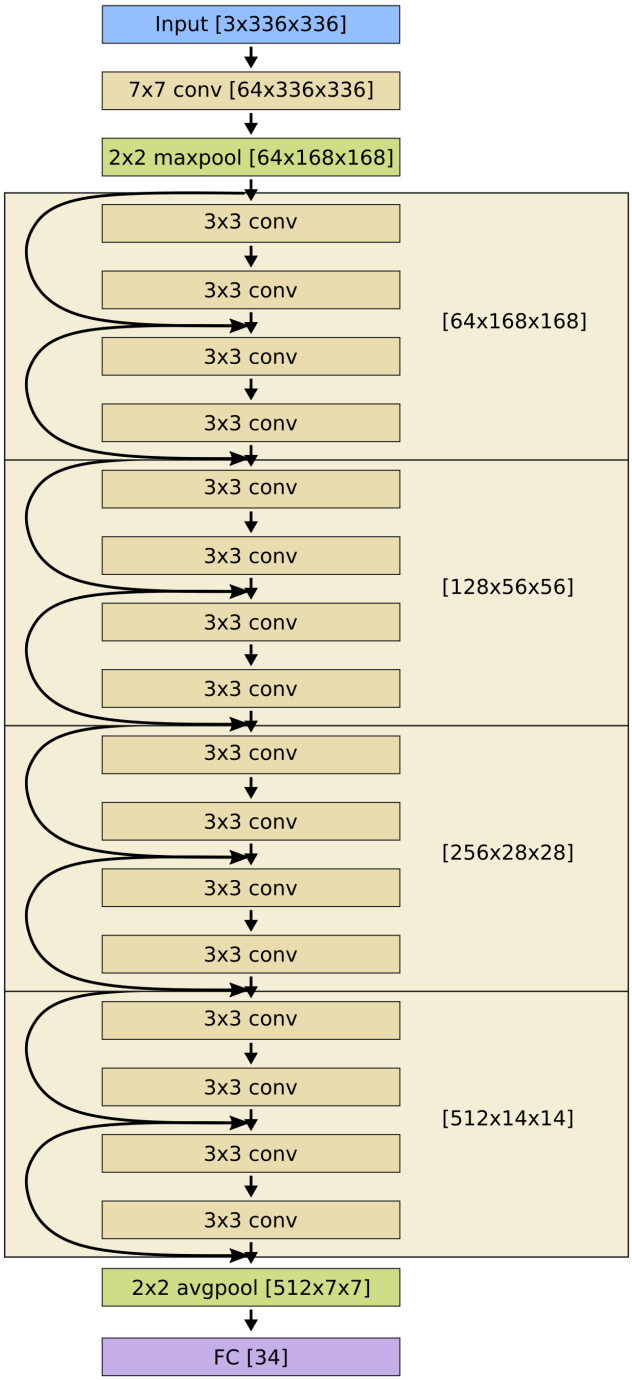

Figure 3.5: Neural network architecture used in this experiment, based on an 18 layer ResNet model with decreased down-sampling in the early layers. 112x112 image is upsampled to 336x336 using bilinear interpolation before being input in to neural network.

coefficients, we can also calculate the RMS wavefront error as,

$$RMS = \left(\sum_{j=3}^{N} c_j^2 \right)^{1/2}, \tag{3.2}$$

where c_j is the coefficient corresponding to the Zernike polynomial $\mathcal{Z}_j$ [14]. As shown in Figure 3.7, a higher RMS value generally corresponds to a more highly aberrated focus. For both metrics, we have defined the improvement of the corrected focus over the aberrated focus. For the spot metric, the improvement is defined as

$$\eta_s = \frac{\mathcal{S}_{corrected}}{\mathcal{S}_{aberrated}}, \tag{3.3}$$

and for the RMS error,

$$\eta_{_{RMS}} = \frac{RMS_{aberrated}}{RMS_{corrected}}. \tag{3.4}$$

For both improvement metrics, a higher value corresponds to a bigger improvement of the corrected focus over the aberrated focus.

3.3 Results and Discussion

3.3.1 Dataset Size

In optimizing the training of our model on the dataset, we first looked at the effect of dataset size on prediction performance and convergence of the network. For this, we trained the network on a subset of the Zernike polynomials $\mathcal{Z}_2 - \mathcal{Z}_9$ on datasets ranging from 100k-1000k examples. The results are shown in Figure 3.8.

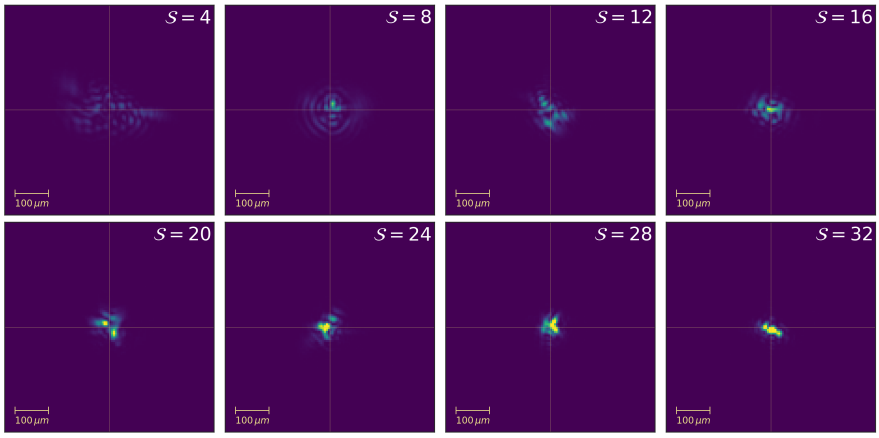

Figure 3.6: Examples of the spot sharpness metric applied to a range of aberrated focus images from the training dataset.

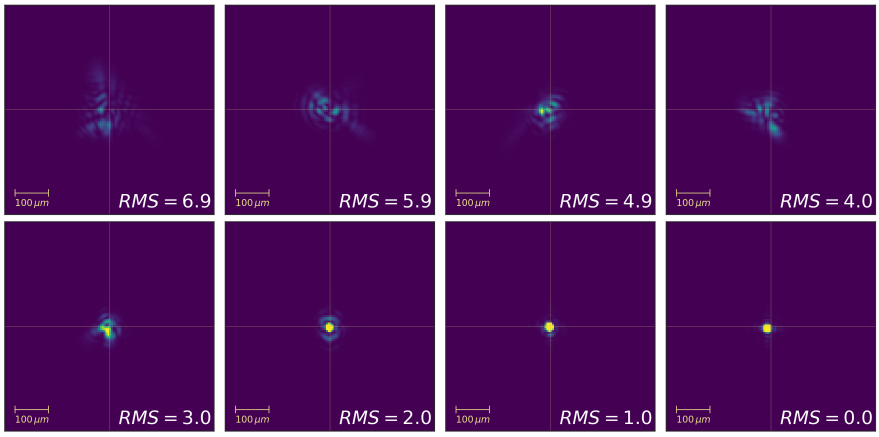

Figure 3.7: Examples of the RMS wavefront error calculated for a range of aberrated focus images from the training dataset.

You can see that the RMSE test loss drastically decreases between 240k and 450k examples. [2]

In Figure 3.9 below, you can see that training the model on a dataset smaller than 800k examples leads to sub-optimal performance on the validation set and significant over-fitting on the training set. The over-fitting issue is not overcome until the dataset is nearly 1 million examples.

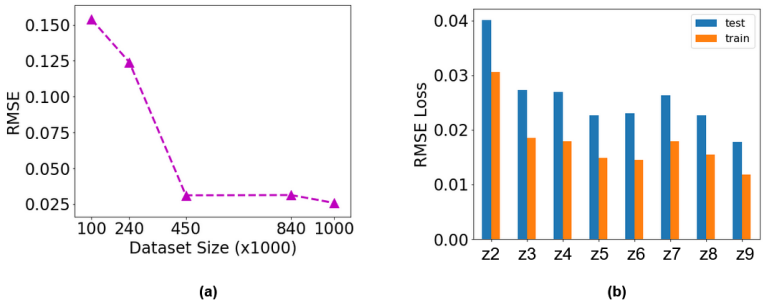

Figure 3.8: RMSE test loss for trained CNN model. (a) RMSE test loss as a function of dataset size. (b) RMSE loss for each of the Zernike Polynomials $\mathcal{Z}_2 - \mathcal{Z}_9$ using our best model trained on 1 million examples in the dataset size test.

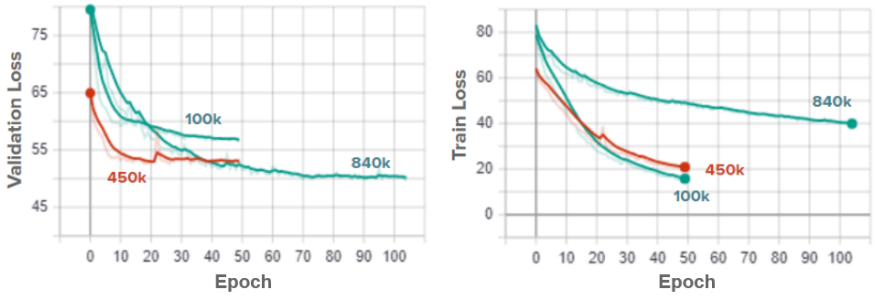

Figure 3.9: RMSE validation loss (top) and training loss (bottom) during training for datasets with 100k, 450k, and 840k examples.

[2] All values of RMSE loss have been normalized to the the wavelength λ.

For the 1M example dataset, we looked at the loss per Zernike polynomial. In Figure 3.8, it is clear that aberrations caused by the first Zernike polynomial are the least predictive. This is interesting, because the first two polynomials correspond to horizontal and vertical translation, so we would not expect to see a major difference in the ability of the network to predict their effects. Otherwise, the loss is fairly consistent across the polynomials, which is a good sign for the training regime.

3.3.2 Experimental Aberration Correction

After training the CNN model on the full dataset of 8M examples, we tested the ability of the network to correct for aberrations on our experimental setup. To do so, we loaded the modulation mask represented by a set of aberration coefficients c_a onto the SLM (see Figure 3.3) and collected the resulting aberrated focus image. We then fed the image into the CNN model, which returns the predicted coefficients c_p for Zernike Polynomials $\mathcal{Z}_2 - \mathcal{Z}_{35}$ responsible for the aberration. To test the correction, we then calculate the residual coefficients $c_r = c_a - c_p$. Finally, we load the residual coefficients onto the SLM and collect the corrected focus image. A visualization of the focus intensity patterns for this process is shown in Figure 3.4. A visualization of the coefficients c_r, c_a, c_p are shown in Figure 3.11.

We repeated this process over a random subset of 4000 aberrations in the validation dataset, with the results displayed as in Figure 3.12. The corrected focus images are focused quite well compared to the aberrated focus image for

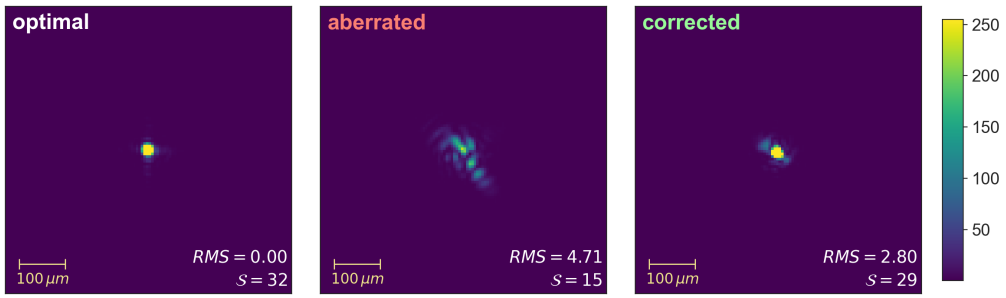

Figure 3.10: The focus intensity patterns for the CNN aberration correction experiment where the correction takes place on the experimental setup. Focus intensity patterns are shown for the unaberrated focus, the aberrated focus, and the corrected focus. The spot sharpness metric and RMS wavefront error are displayed for each image.

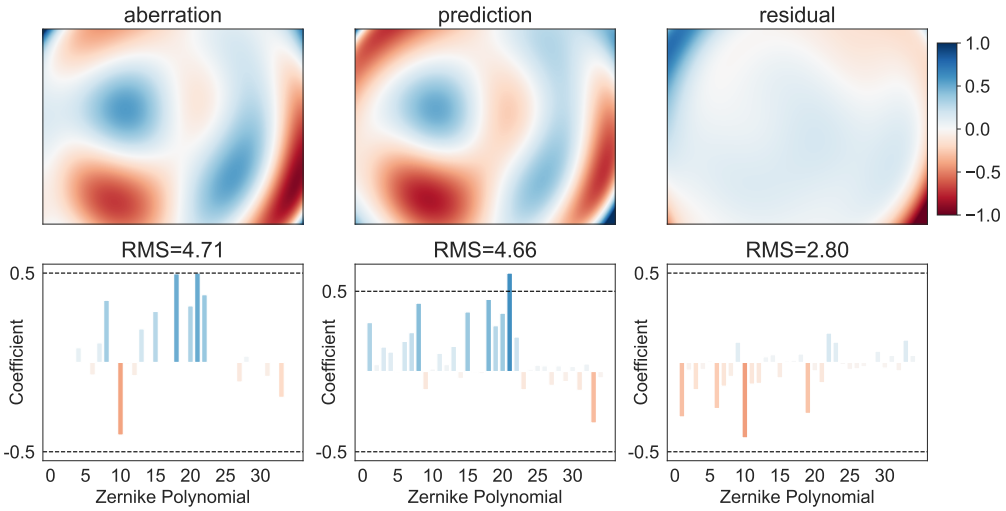

Figure 3.11: Aberrated, predicted, and residual (aberrated - predicted) coefficients the CNN aberration correction experiment. The corresponding phase masks are shown above. The RMS wavefront error is displayed for each set of coefficients.

all randomly chosen examples shown.[3] Histograms of the RMS wavefront error and the spot metric normalized by the optimal focus spot metric $\mathcal{S}_{optimal}$ for the aberrated and corrected focus images are also shown. The distribution of the corrected metrics show clear improvement, with an average RMS improvement $\eta_{RMS} = 1.7$ and an average spot metric improvement $\eta_s = 2$.

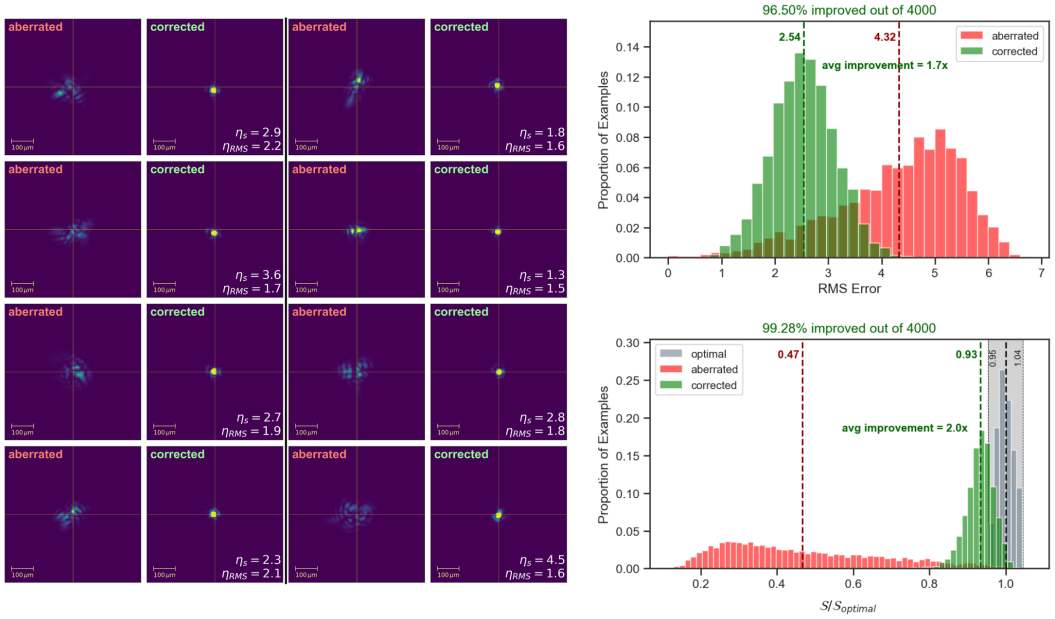

Figure 3.12: Experimental correction results of 4000 simulated aberrations from the validation dataset. (left) Examples of aberrated and corrected focus intensity field pairs from the CNN correction experiment with improvement metrics for RMS wavefront error and spot sharpness metric displayed for each corrected focus image. Coefficients describing aberrations are randomly chosen from the validation dataset, and therefore were never used to train the neural network. The cross-hairs indicate the approximate unaberrated center of focus. (right) Histograms of the RMS wavefront error and the spot metric normalized by the optimal focus spot metric $\mathcal{S}_{optimal}$ for the aberrated and corrected focus images.

[3]These results represent preliminary experimental data, and a more rigorous statistical analysis of the CNN model's correction performance will be the next step in this work.

Next, we repeated this process over a set of 8000 new, randomly generated coefficients, with the results displayed as in Figure 3.13. Notice that even though the aberration coefficients were not part of the training or validation dataset, the neural network is able to correct the aberrated image to a high degree for all randomly chosen examples shown. Histograms of the RMS wavefront error and the spot metric normalized by the optimal focus spot metric $\mathcal{S}_{optimal}$ for the aberrated and corrected focus images are also shown. The distribution of the corrected metrics show clear improvement, with an average RMS improvement $\eta_{RMS} = 1.8$ and an average spot metric improvement $\eta_s = 3$.

3.4 Conclusion

In this work, we created a dataset and trained a convolutional neural network CNN regression model to predict the Zernike correction to aberrations in an optical system. The model that we used was based on an 18 layer ResNet architecture. We trained the model on a dataset of eight million examples of simulated aberrations using Zernike Polynomials $\mathcal{Z}_2 - \mathcal{Z}_{35}$. After the model was trained, we tested it experimentally by using the SLM to create new aberrations, correcting them using predicted coefficients from the trained model, and comparing the aberrated and corrected focus intensity patterns that result. We presented preliminary results from this experiment, which show that the trained CNN model is able to achieve a high degree of correction on new, randomly generated optical aberrations.

To take this work further, we plan to complete a more rigorous statistical

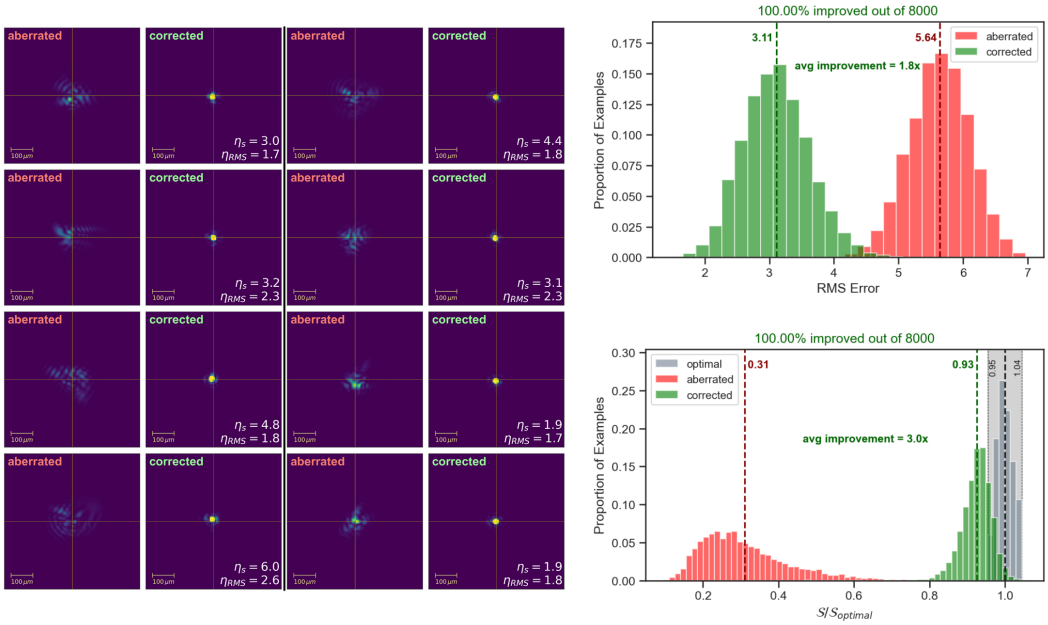

Figure 3.13: Experimental correction results of 8000 new, randomly generated aberrations. (left) Examples of aberrated and corrected focus intensity field pairs from the CNN correction experiment with improvement metrics for RMS wavefront error and spot sharpness metric displayed for each corrected focus image. Coefficients describing aberrations were not part the training or validation dataset. The cross-hairs indicate the approximate unaberrated center of focus. (right) Histograms of the RMS wavefront error and the spot metric normalized by the optimal focus spot metric $\mathcal{S}_{optimal}$ for the aberrated and corrected focus images.

analysis of the CNN model's correction performance on simulated aberrations. We also have begun exploratory tests of our model correcting for real sample aberrations. We are most interested in the performance of our model on dynamic media such as living tissue. We intend to test the ability of the model to maintain a focus through moving materials and turbulent liquids. Because the correction takes place on the scale of milliseconds, these results represent an indication of the exciting potential of neural networks to advance the field of optical aberration correction into previously unreachable aberration domains.

Bibliography

[1] M. J. Booth, "Adaptive optics in microscopy," *Philosophical Transactions of the Royal Society A: Mathematical, Physical and Engineering Sciences*, vol. 365, pp. 2829–2843, Dec. 2007.

[2] F. Roddier, ed., *Adaptive Optics in Astronomy*. Cambridge: Cambridge University Press, 1999.

[3] M. J. Booth, M. A. A. Neil, R. Juškaitis, and T. Wilson, "Adaptive aberration correction in a confocal microscope," *Proceedings of the National Academy of Sciences*, vol. 99, pp. 5788–5792, Apr. 2002. Publisher: National Academy of Sciences Section: Physical Sciences.

[4] N. Ji, D. E. Milkie, and E. Betzig, "Adaptive optics via pupil segmentation for high-resolution imaging in biological tissues," *Nature Methods*, vol. 7, pp. 141–147, Feb. 2010. Number: 2 Publisher: Nature Publishing Group.

[5] M.-C. Zhong, X.-B. Wei, J.-H. Zhou, Z.-Q. Wang, and Y.-M. Li, "Trapping red blood cells in living animals using optical tweezers," *Nature Communications*, vol. 4, pp. 1–7, Apr. 2013.

[6] M.-C. Zhong, Z.-Q. Wang, and Y.-M. Li, "Aberration compensation for optical trapping of cells within living mice," *Applied Optics*, vol. 56, pp. 1972–1976, Mar. 2017.

[7] I. M. Vellekoop and A. P. Mosk, "Focusing coherent light through opaque strongly scattering media," *Optics Letters*, vol. 32, pp. 2309–2311, Aug. 2007.

[8] J. W. Goodman, *Statistical Optics.* John Wiley & Sons, 2000.

[9] I. M. Vellekoop, E. G. v. Putten, A. Lagendijk, and A. P. Mosk, "Demixing light paths inside disordered metamaterials," *Optics Express*, vol. 16, pp. 67–80, Jan. 2008.

[10] T. Čižmár, "Imaging through Turbid Media," in *Classical Optics 2014 (2014), paper CW1C.2*, p. CW1C.2, Optical Society of America, June 2014.

[11] T. Čižmár, M. Mazilu, and K. Dholakia, "*In situ* wavefront correction and its application to micromanipulation," *Nature Photonics*, vol. 4, pp. 388–394, June 2010.

[12] A. P. Mosk, A. Lagendijk, G. Lerosey, and M. Fink, "Controlling waves in space and time for imaging and focusing in complex media," *Nature Photonics*, vol. 6, pp. 283–292, May 2012.

[13] I. M. Vellekoop, "Feedback-based wavefront shaping," *Optics Express*, vol. 23, pp. 12189–12206, May 2015.

[14] V. Lakshminarayanan and A. Fleck, "Zernike polynomials: a guide," *Journal of Modern Optics*, vol. 58, pp. 1678–1678, Oct. 2011. Publisher: Taylor & Francis _eprint: https://doi.org/10.1080/09500340.2011.633763.

[15] Y. Jin, Y. Zhang, L. Hu, H. Huang, Q. Xu, X. Zhu, L. Huang, Y. Zheng, H.-L. Shen, W. Gong, and K. Si, "Machine learning guided rapid focusing with sensor-less aberration corrections," *Optics Express*, vol. 26, pp. 30162–30171, Nov. 2018.

[16] Y. Nishizaki, M. Valdivia, R. Horisaki, K. Kitaguchi, M. Saito, J. Tanida, and E. Vera, "Deep learning wavefront sensing," *Optics Express*, vol. 27, pp. 240–251, Jan. 2019.

[17] Q. Tian, C. Lu, B. Liu, L. Zhu, X. Pan, Q. Zhang, L. Yang, F. Tian, and X. Xin, "DNN-based aberration correction in a wavefront sensorless adaptive optics system," *Optics Express*, vol. 27, pp. 10765–10776, Apr. 2019. Publisher: Optical Society of America.

[18] M. Wang, M. Wang, W. Guo, and X. Yuan, "Single-shot wavefront sensing with deep neural networks for free-space optical communications," *Optics Express*, vol. 29, pp. 3465–3478, Feb. 2021. Publisher: Optical Society of America.

[19] J. C. Wyant and K. Creath, "Basic Wavefront Aberration Theory for Optical Metrology," vol. 11, p. 2, 1992. Conference Name: Applied Optics and Optical Engineering, Volume XI.

[20] J. L. M. Fuentes, E. J. Fernández, P. M. Prieto, and P. Artal, "Interferometric method for phase calibration in liquid crystal spatial light modulators using a self-generated diffraction-grating," *Optics Express*, vol. 24, pp. 14159–14171, June 2016.

[21] T. P. Moffitt, Y.-C. Chen, and S. A. Prahl, "Preparation and characterization of polyurethane optical phantoms," *Journal of Biomedical Optics*, vol. 11, p. 041103, July 2006. Publisher: International Society for Optics and Photonics.

[22] U. Sukowski, F. Schubert, D. Grosenick, and H. Rinneberg, "Preparation of solid phantoms with defined scattering and absorption properties for optical tomography," *Physics in Medicine and Biology*, vol. 41, pp. 1823–1844, Sept. 1996.

[23] B. W. Pogue and M. S. Patterson, "Review of tissue simulating phantoms for optical spectroscopy, imaging and dosimetry," *Journal of Biomedical Optics*, vol. 11, p. 041102, July 2006.

[24] M. Firbank and D. T. Delpy, "A design for a stable and reproducible phantom for use in near infra-red imaging and spectroscopy," *Physics in Medicine and Biology*, vol. 38, pp. 847–853, June 1993.

[25] J. C. Christou, K. J. Mighell, and R. B. Makidon, "Strehl ratio and image sharpness for adaptive optics," in *Advances in Adaptive Optics II*, vol. 6272, p. 62721Y, International Society for Optics and Photonics, June 2006.

[26] B.-J. Seo, C. Nissly, G. Angeli, B. Ellerbroek, J. Nelson, N. Sigrist, and M. Troy, "Analysis of normalized point source sensitivity as a performance metric for large telescopes," *Applied Optics*, vol. 48, pp. 5997–6007, Nov. 2009. Publisher: Optical Society of America.

[27] D. B. Conkey, A. N. Brown, A. M. Caravaca-Aguirre, and R. Piestun, "Genetic algorithm optimization for focusing through turbid media in noisy environments," *Optics Express*, vol. 20, pp. 4840–4849, Feb. 2012.

[28] I. M. Vellekoop and A. P. Mosk, "Phase control algorithms for focusing light through turbid media," *Optics Communications*, vol. 281, pp. 3071–3080, June 2008.

[29] Z. Fayyaz, N. Mohammadian, M. Tabar, R. Manwar, and M. Avanaki, "A Comparative Study of Optimization Algorithms for Wavefront Shaping," *Journal of Innovative Optical Health Sciences*, vol. 12, Apr. 2019.

[30] V. Marx, "Microscopy: hello, adaptive optics," *Nature Methods*, vol. 14, pp. 1133–1136, Dec. 2017.

[31] Y. Rivenson, Z. Göröcs, H. Günaydin, Y. Zhang, H. Wang, and A. Ozcan, "Deep learning microscopy," *Optica*, vol. 4, pp. 1437–1443, Nov. 2017. Publisher: Optical Society of America.

[32] Y. He, Y. He, Z. Liu, Z. Liu, Z. Liu, Y. Ning, Y. Ning, J. Li, J. Li, X. Xu, X. Xu, Z. Jiang, and Z. Jiang, "Deep learning wavefront sensing method for

Shack-Hartmann sensors with sparse sub-apertures," *Optics Express*, vol. 29, pp. 17669–17682, May 2021. Publisher: Optical Society of America.

[33] S. Hu, L. Hu, B. Zhang, W. Gong, and K. Si, "Simplifying the detection of optical distortions by machine learning," *Journal of Innovative Optical Health Sciences*, vol. 13, p. 2040001, May 2020. Publisher: World Scientific Publishing Co.

[34] R. A. Muller and A. Buffington, "Real-time correction of atmospherically degraded telescope images through image sharpening," *JOSA*, vol. 64, pp. 1200–1210, Sept. 1974. Publisher: Optical Society of America.